

<https://helda.helsinki.fi>

---

## Chayka, Ivan F. (2023) Volcano Plutonic Complex of the Tumrok Range (Kamchatka): An Example of the Ural-Alaskan Type Intrusion and Related Volcanic Series

Chayka, Ivan F.

Multidisciplinary Digital Publishing Institute

2023-01-15

---

Chayka, I.F.; Baykov, N.I.; Kamenetsky, V.S.; Kutyrev, A.V.; Pushkarev, E.V.; Abersteiner, Ivan F.; Shcherbakov, V.D. Volcano Plutonic Complex of the Tumrok Range (Kamchatka): An Example of the Ural-Alaskan Type Intrusion and Related Volcanic Series. *Minerals* 2023, 13, 126.

---

<http://hdl.handle.net/10138/353323>

---

*Downloaded from Helda, University of Helsinki institutional repository.*





*This is an electronic reprint of the original article.*

*This reprint may differ from the original in pagination and typographic detail.*

*Please cite the original version.*

## Article

# Volcano–Plutonic Complex of the Tumrok Range (Eastern Kamchatka): An Example of the Ural-Alaskan Type Intrusion and Related Volcanic Series

Ivan F. Chayka <sup>1,\*</sup> , Nikolay I. Baykov <sup>1,2</sup>, Vadim S. Kamenetsky <sup>1,3</sup> , Anton V. Kutyrev <sup>4</sup> , Evgenii V. Pushkarev <sup>5</sup> , Adam Abersteiner <sup>6,7</sup> and Vasily D. Shcherbakov <sup>2</sup>

<sup>1</sup> Korzhinskii Institute of Experimental Mineralogy, Russian Academy of Sciences, 142432 Chernogolovka, Russia

<sup>2</sup> Geological Department, Moscow State University, 119991 Moscow, Russia

<sup>3</sup> Institute of Volcanology and Seismology, Far East Branch of Russian Academy of Sciences, 683000 Petropavlovsk-Kamchatsky, Russia

<sup>4</sup> Department of Earth Sciences, University of Oregon, Eugene, OR 97403, USA

<sup>5</sup> Zavaritsky Institute of Geology and Geochemistry, Ural Branch of Russian Academy of Sciences, 620016 Yekaterinburg, Russia

<sup>6</sup> Institute of Sustainability, Energy and Resources (ISER), The University of Adelaide, Adelaide 5005, Australia

<sup>7</sup> Department of Earth Sciences, The University of Adelaide, Adelaide 5005, Australia

\* Correspondence: ivanlab211@gmail.com; Tel.: +7-913-772-3224

**Abstract:** Zoned plutons, composed of dunites, pyroxenites, and gabbroic rocks, have been referred to as the Ural-Alaskan type complexes (UA-complexes) and occur in numerous paleo-arc settings worldwide. Many of these complexes are source rocks for economic placers of platinum-group metals. Thus, it is important to understand how UA-complexes form and the origin and behavior of platinum-group elements (PGEs). It is widely assumed that the UA-complexes result from differentiation of supra-subduction high-Ca high-Mg sub-alkaline magmas. However, there is a lack of direct evidence for the existence and differentiation of such magmas, mainly because cases of UA-complexes being spatially and temporally linked to co-genetic volcanics are unknown. We studied an UA-complex from the Tumrok range (Eastern Kamchatka) where a dunite-clinopyroxenite-gabbro assemblage is spatially and temporary related to high-Ca volcanics (i.e., picrites and basalts). Based on the mineral and chemical composition of the rocks, mineral chemistry, and composition of melt inclusions hosted within rock-forming minerals, we conclude that the intrusive assemblage and the volcanics are co-genetic and share the same parental magma of ankaramitic composition. Furthermore, the compositions of the plutonic rocks are typical of UA-complexes worldwide. Finally, the rocks studied exhibit a full differentiation sequence from olivine-only liquidus in picrites and dunites to eutectic crystallization of diopside or hornblende, plagioclase, and K-Na feldspar in plagioclase-wehrlites and gabbroic rocks. All these results make the considered volcano–plutonic complex a promising case for petrological studies and modelling of UA-complex formation.

**Keywords:** Ural-Alaskan type complex; ankaramite; picrite; basalt; wehrlite; Eastern Kamchatka; melt inclusions; magma differentiation; arc magmatism



**Citation:** Chayka, I.F.; Baykov, N.I.; Kamenetsky, V.S.; Kutyrev, A.V.; Pushkarev, E.V.; Abersteiner, A.; Shcherbakov, V.D. Volcano–Plutonic Complex of the Tumrok Range (Eastern Kamchatka): An Example of the Ural-Alaskan Type Intrusion and Related Volcanic Series. *Minerals* **2023**, *13*, 126. <https://doi.org/10.3390/min13010126>

Academic Editor: Jaroslav Dostal

Received: 9 December 2022

Revised: 4 January 2023

Accepted: 12 January 2023

Published: 15 January 2023



**Copyright:** © 2023 by the authors. Licensee MDPI, Basel, Switzerland. This article is an open access article distributed under the terms and conditions of the Creative Commons Attribution (CC BY) license (<https://creativecommons.org/licenses/by/4.0/>).

## 1. Introduction

Mafic-ultramafic plutons, composed of dunites, clinopyroxenites, and gabbroic rocks, that have a concentrically-zoned structure, largely occur within supra-subduction settings and are referred to as “Ural-Alaskan-type complexes” (hereinafter UA-complexes) [1–5]. Their occurrences are widespread in SE Alaska and British Columbia [3,6–11] and the Ural mountains [2,12–22], and are also recognized in the Koryak Highlands and Kamchatka [1,23–28], Venezuela [29], New South Wales [30,31], New Zealand [32], Siberia [2,33,34], Northwestern Africa and Saudi Arabia [35,36], and the Superior Province (Canada) [37]. Typical rock

assemblages of UA-complexes include a dunitic core, surrounded by wehrlitic and clinopyroxenitic rocks, and hornblende-rich and gabbroic assemblages [1–3,6,10,15,17,29,36]. These complexes are of significant economic interest, as they may be the source of placer and bedrock deposits of platinum-group elements (PGEs) [2,9,10,13,16,27,34,38–42].

Since their discovery in the Urals and Alaska [4,43,44], the origin of UA-complexes has been a subject of debate. The earliest systematic petrological studies of the Alaskan zoned intrusions [3] suggested that these complexes were formed from several pulses of high-Mg, high-Ca, and low-Si magmas (magmatic mushes). Further studies considered UA-complexes to be layered intrusions, formed either in situ [10,23] or subjected to post-solidus diapiric re-emplacement [8]. They were also considered feeder conduits for the andesitic volcanos where dynamic differentiation of the crystallizing magma gave rise to the zoned structure of the complexes [6,15,29], or magmatic diapirs, ascending from lithospheric mantle [2,45]. The proposed compositions of the parental melts for the UA-complexes include subalkaline orthopyroxene-normative island-arc basalts [6,29,46], high-Ca-Mg alkaline ultramafic [8,47], shoshonitic [30], or alkaline to subalkaline high-Ca/Al high-Mg (ankaramitic) [1,7,19,48–50].

Recognition of the melts that gave rise to UA-complexes remains challenging, particularly because these complexes are not directly linked with any effusive series rocks, which could provide useful insights into the composition of such melts. Existing estimates are based on bulk rock compositions [8,19,51], the abundances and compositions of cumulate minerals, melt/crystal partitioning coefficients [1,18,48,49,51,52], and melt inclusion studies [32,53]. Comparative studies, which have considered UA-complexes and their supposedly coeval effusive rock equivalents, were conducted by Irvine (1973), Tistl et al. (1994), and Batanova et al. (2005) [1,7,11]. The latter study considered the Galmoenan complex of the Koryak highlands (Northern Kamchatka) and proposed that its parental melt was close to that of the Tumrok range volcanics (Eastern Kamchatka). However, despite being coeval and occurring within the same Olyutorsky arc terrane [1,54,55], these occurrences are more than 600 km away from each other and cannot be considered bona fide co-genetic. On the other hand, a plutonic body composed of dunites, wehrlites, and gabbroic rocks has been described in close spatial connection with the Tumrok range volcanics [56–59]. Its rock assemblage and supposedly zoned structure [56] resembles UA-complexes, thereby making this occurrence an interesting potential case of a UA-complex that is closely linked to a volcanic series.

In this study, we present a detailed geological, petrographical, mineralogical, and compositional description of this intrusion and related volcanic rocks, give new data on chromite-hosted melt inclusions, and discuss co-magmatism of the effusive and intrusive varieties. Furthermore, we place novel constraints on their parental melt composition, its differentiation, and the evolution of these series. We compared these rocks with those from typical UA-complexes worldwide to test whether this occurrence may be considered as a “model case” for studying the petrology of UA-complexes.

## 2. Geological Background and Field Observations

The Tumrok Range volcanic province is composed of basaltic, picritic, and volcanoclastic rocks of the Valaginsky series [59–63] and several plutonic occurrences. This province belongs to the Achaivayam-Valaginsky (syn. Olyutorsky) island-arc terrane ( $K_2-P_1$ ), which also includes the Valaginsky range (another large occurrence of picritic and basaltic rocks), and is part of the Koryak Highlands, hosting Galmoenan and Epilchik UA-complexes [1,23,26,55] (Figure 1A).

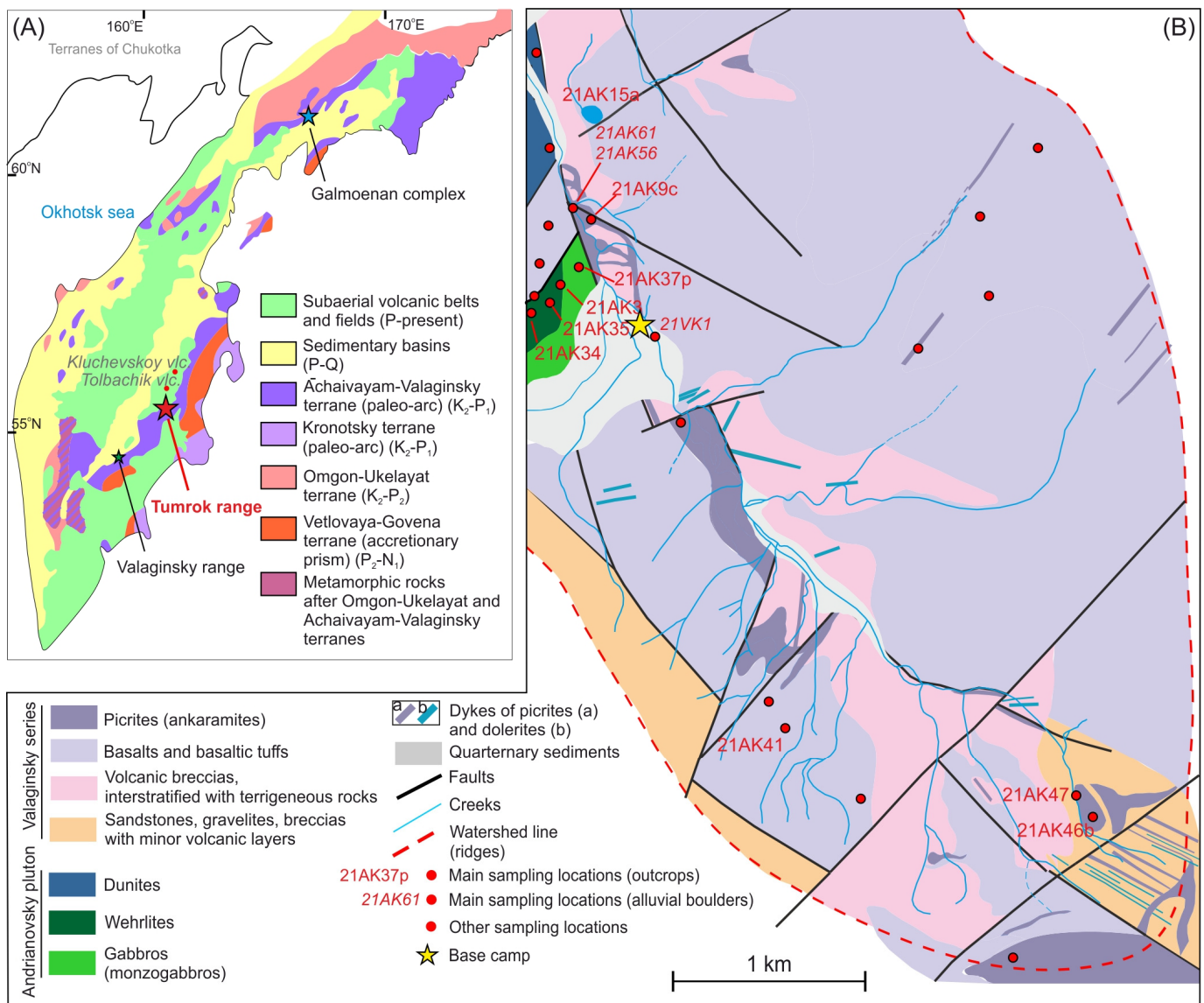


**Figure 1.** Geological setting of the studied complex. (A) Geological map of Kamchatka peninsula (after [55]); (B) geological scheme of the studied occurrence (after unpublished sketch of B. A. Markovskiy with the authors' editions).

The 75–80 Ma Valaginsky volcanic series [58,59] is composed (bottom up) of volcano-sedimentary rocks, volcanic breccias and basalt lava flows, picrites, and picritic tuffs. The effusive series is cross-cut basaltic and picritic dykes. The latter also occurs as sills hosted by effusive rocks of the Valaginsky series, so it is difficult to distinguish between the different volcanic and sub-volcanic facies of picrites. The 70–80 Ma [64] plutonic complex is represented by ultramafic-gabbro and gabbro-syenitic intrusions sized 2–8 km<sup>2</sup> and is largely localized at the base of the Valaginsky series [63]. The intrusions were supposed to be layered with dominant gabbroic rocks and subordinate ultramafics. Furthermore, certain studies advocated close genetic links between this complex and volcanic ultramafics [58,59,63].

The studied occurrence (Figure 1B) is located in a cirque of the Shumniy Creek (Figure 2A,B) at the Northwestern slope of the Tumrok Range and is dominated by basalts and subordinate picrites. The latter, according to [59], form sills and occasional dykes, yet it is not excluded that some of these picrites may be bona fide effusive. Rocks of the plutonic complex are found at the Western sector of the studied area and are part of the

Andrianovsky pluton [59,63], which was supposed to have a concentrically zoned structure, similar to that of UA-complexes [56]. The intrusive rocks are represented by dunites, wehrlites, and gabbros (Figure 1B). Contacts between the intrusion and host Valaginsky series are obscured. However, based on structural and tectonic features of the area, it has been supposed that the intrusive complex is bounded by subvertical faults [59] (Figure 1B).

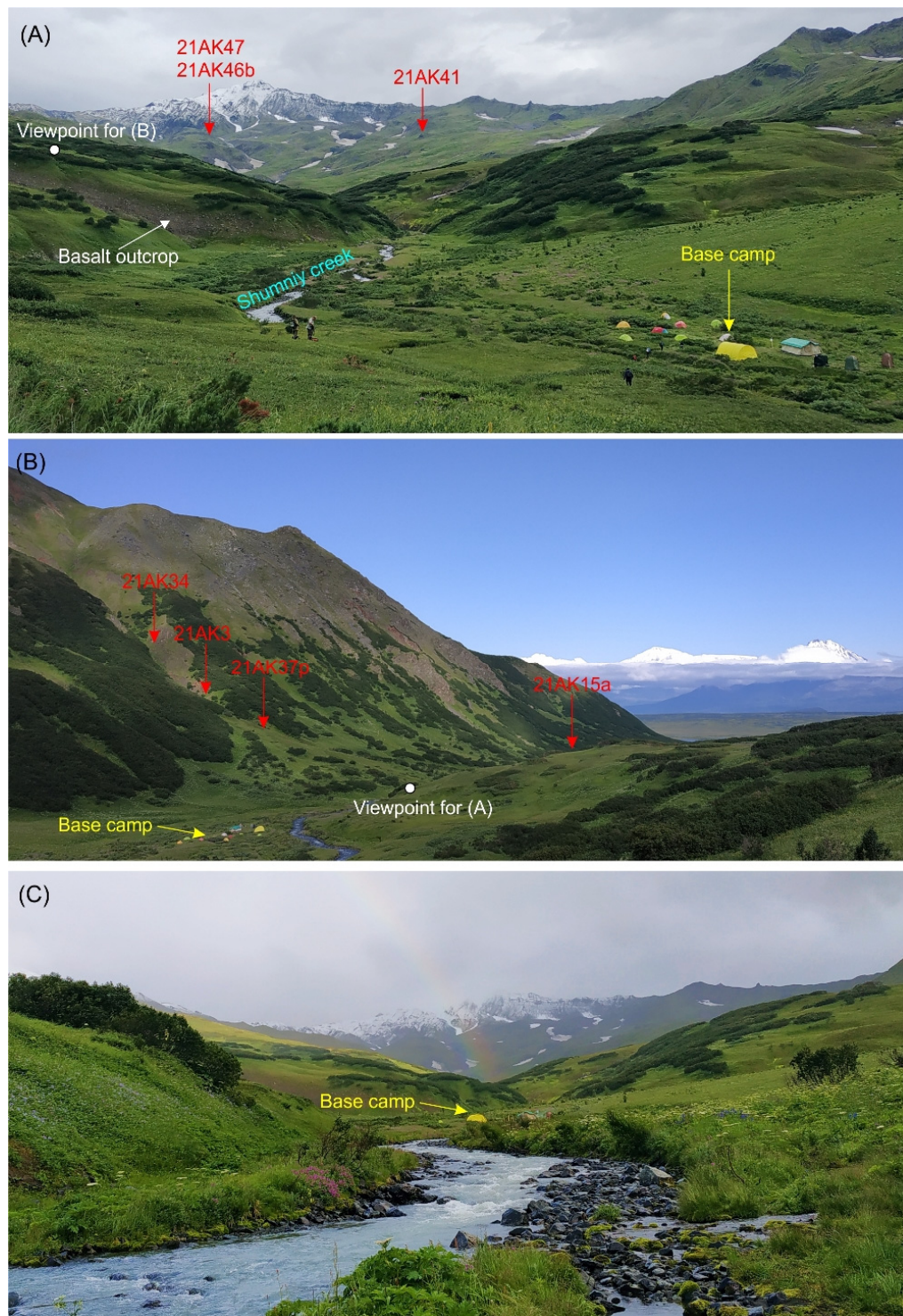


**Figure 2.** Photographs of the studied occurrence. (A) Southeastern view; (B) Northwestern view; (C) stream of the Shumny creek with boulders in the alluvium. Sampling locations are labeled red.

Our field observations support the dominance of basalts and picrites in the study area. Occurrences of wehrlites and gabbros of the Andrianovsky pluton are restricted to a gorge, which crosses the southwestern ridge of the cirque (Figure 2B), and dunites occur within a small area at the outlet of the cirque. In addition, all rock varieties, except dunites, are found in the alluvium of Shumnyy Creek (Figure 2C), where they are better preserved than in the bedrock outcrops. Abundant outcrops of picrites with characteristic comb-like weathering (Figure 3A,B) are found at the upper part of the cirque, where they are thought to form thick sills [59]. Basalts and basaltic tuffs are common at the brinks of the Shumnyy Creek. However, the best outcrops of basalts (Figure 3C), differentiated top down from aphyric amygdaloidal to holocrystalline varieties, are found at the slopes of the cirque. Occurrences of the intrusive rocks are heavily weathered and are mostly recognized by their distinct predominance in eluvium (Figure 3D), whereas serpentinized dunites were found as outcrops at the brink of the Shumnyy Creek (Figure 3E).



**Figure 3.** Field photographs of the outcrops with the labeled samples. (A) comb-like weathered bedrock picrite; (B) olivine phenocrysts on a water-polished surface of picrite; (C) an outcrop of a differentiated basalt flow; (D) a boulder of breccia-like gabbroic rock; (E) an outcrop of weathered dunite, Shumnyy creek brink. Photograph (E) is by Elizaveta Grigor'eva.

### 3. Samples and Methods

Sampling was performed on both bedrock outcrops and alluvial boulders at Shumnyy Creek (Figure 1B). The latter approach allowed for the collection of better-preserved rocks than from outcrops, which were typically strongly weathered. The presence of only Valagin-sky volcanics and rocks of the Andrianovsky pluton was ensured by the fact that the basin of the Shumnyy Creek is restricted to only the studied cirque, bounded by the watershed

ridges (Figure 1B). In addition, a single sample (Tu-25) was taken from the 1980s collection of Kamenetsky V.S. (its chemical composition is reported in [54]). Polished thin sections and epoxy mounts with the rock chips were prepared for optical microscopy, electron microscopy, and microprobe analyses.

Heating and homogenization of Cr-spinel-hosted melt inclusions was performed using a custom-designed tube furnace in Institute of Experimental Mineralogy RAS, analogous to that described in [65]. The experimental setup consisted of an insulated sapphire tube, wired by a kanthal heater, a temperature controller, and a Pt container for the inclusion-bearing grains. For the experiment, grains of Cr-spinel were separated from the crushed rock sample and placed into the Pt container along with pure metallic Fe, which acted as a buffer, preventing oxidation of the Cr-spinel grains. The container was loosely sealed and placed into the tube, which then was gradually heated up to 1250 °C. After 10 min of heating, the container was dropped into water so that the estimated time of cooling from 1250 °C to room temperature was no more than 3 s. The grains were then mounted into an epoxy mount, grinded, and polished. The exposed melt inclusions were analyzed by EPMA.

Instrumental methods included scanning electron microscopy with energy dispersive microanalysis (SEM-EDS), X-ray wavelength dispersive electron microprobe analysis (EPMA), and bulk major and trace element chemical analysis of the rocks: X-ray fluorescence analysis of major components, Cr<sub>2</sub>O<sub>3</sub> and TiO<sub>2</sub>, and mass spectrometry with inductively-coupled plasma ionization (ICP-MS).

SEM-EDS investigation was carried out on (1) Tescan VEGA-II XMU INCA Energy 450 (Korzhinskii Institute of Experimental Mineralogy Russian Academy of Sciences—IEM RAS, Chernogolovka, Russia), (2) Tescan Mira 3 LMU with Oxford INCA Energy XMax 80 detector for EDS analysis (Analytical Center for multi-elemental and isotope research SB RAS), and (3) JEOL JSM-6480LVIT-500 scanning electron microscope with an Oxford XMaxN EDS analyzer (Laboratory of Analytical Techniques of High Spatial Resolution Laboratory of Local Methods of Matter Study, Department of Geology, Moscow State University).

Analyses of olivine, Cr-spinel, clinopyroxene, and Cr-spinel-hosted inclusions were obtained using an electron microprobe JEOL JXA-8230 (Laboratory of Analytical Techniques of High Spatial Resolution, Department of Geology, Moscow State University). Olivine was analyzed at accelerating voltage 20 kV and beam current 300 nA with a beam size of 3 μm, Cr-spinel—at 20 kV and 70 nA, clinopyroxene—at 20 kV and 100 nA, Cr-spinel-hosted inclusions—at 20 kV and 10 nA using a defocused beam to minimize effect of migration of glass components [66]. Primary reference materials for Cr-spinel were chromite NMNH 117075, gahnite NMNH 145883, diopside NMNH 117744, synthetic NiO, V<sub>2</sub>O<sub>3</sub>, and MnTiO<sub>3</sub>. Ilmenite (NMNH 96189) and chromite (NMNH 117075) were used as secondary standards for the analysis quality control. Primary references for olivine were San Carlos olivine (SCOL, NMNH 111312-44), synthetic Cr<sub>2</sub>O<sub>3</sub>, NiO, Al<sub>2</sub>O<sub>3</sub>, MnTiO<sub>2</sub>, and CaSiO<sub>3</sub>. MongOl olivine [67] was used as a secondary standard. Primary references for clinopyroxene were jadeite, augite NMNH-112142, synthetic MnTiO<sub>3</sub>, NiO, and Cr<sub>2</sub>O<sub>3</sub>. Cr-augite NMNH 164905 was used as a secondary standard. Ferric and ferrous ion abundances in Cr-spinel were rendered from FeO total via charge-deficiency-based recalculation [68].

Bulk-rock X-ray fluorescence analysis has been performed in Institute of the Earth's Crust (IEC SB RAS), Irkutsk using S4 Pioneer (Bruker AXS, Karlsruhe, Germany) wavelength dispersive spectrometer [69]. Bulk-rock ICP-MS analysis was carried out in Analytical Center of the Institute of the Earth Crust on the VG Elemental PlasmaQuad PQ2+ Turbo quadrupole spectrometer following autoclave dissolution of rock powder by HNO<sub>3</sub>, HF, HCl, and HClO<sub>4</sub> acids [70].

## 4. Results

### 4.1. Petrography

Petrographic features, mineral proportions (vol. %), and compositions of a set of representative samples (picrites, basalts, dunites, wehrlites, and gabbroic rocks) are summarized in Table 1.

**Table 1.** Petrographical and mineralogical summary of the main samples studied.

Sample	Rock Name	Texture	Modal Composition (%)	Mg# (Ol)	Mg# (Cpx)
21AK9c	Picrite	Porphyritic	Phenocrysts <sup>1</sup> (50) <sup>2</sup> : Ol <sup>3</sup> (90) Cpx (10) Chr (<1) Groundmass (50): Cpx (60), Srp+Chl+AlkFs (35) Mhbl+Bt (5)	87–89	65–86
21AK58	Picrite	Porphyritic	Phenocrysts (40): Ol (85) Cpx (15) Groundmass (60): Cpx (50), Srp+Chl+AlkFs (45) Mhbl+Bt (5)	86–87	71–90
Tu-25(+)	Picrite	Porphyritic	Phenocrysts (60): Ol (100) Groundmass (40): Cpx (30), Pl+KNaFs (50) Srp+Chl (10) Mhbl+Bt (10)		
21AK9e	Basalt	Porphyritic (seriate)	Phenocrysts (10): Cpx (70) Pl* <sup>2</sup> (30) Groundmass (90): Chl + Or (70), Ab+Or (ps-morphs) (30)		70–89
21AK41	Basalt	Intergranular	Feldspars (40): Cpx (35) Chl+Act (20) Mag+Ap (5)		71–89
21AK61a	Basalt	Porphyritic	Phenocrysts (15): Cpx (90) Ol* (10) Groundmass (85): Chl + Or (70), Ab+Or (ps-morphs) (30) Mag (2)		68–82
21AK15a	Dunite (serpentinized)	Granular, mosaic	Srp (90), Ol (5), Mag (5)	90–91	
21AK47 (xen.)	Dunite	Granular, mosaic	Ol (85), Srp (14), Chr (1)	88–89	
21AK34	Wehrlite	Poikilitic	Ol (55) Cpx (40) Phl (4) CrMag (1)		
21AK3	Wehrlite	Granular, subhedral, poikilitic	Ol (25), Cpx (70) Phl (4) CrMag (1)	80–81	81–88
21AK56	Plagio-wehrlite	Subhedral, poikilitic, consertal	Ol (25), Cpx * (30), Feldspar (10) Bt+Hbl (7) CrMag+Ap(3), Srp+Chl (25)	81–82	78–88
21AK37p	Gabbro (monzogabbro)	Subhedral, intergranular	Cpx * (50) Feldspar (43) Bt (4) Mag (3)		89–92
21VK1	Gabbrodolerite	Poikilo-ophytic	Cpx (25) Feldspar (73) Mag (2)		57–75

<sup>1</sup> For the porphyritic rocks mineral generations are divided into “phenocrysts” and “groundmass”. <sup>2</sup> Numbers in parentheses refer to estimated vol. % of mineral generations (phenocrysts/groundmass) and minerals themselves. <sup>3</sup> Hereinafter, mineral abbreviations are after [71]. An asterisk (\*) after the mineral symbol means that the particular mineral has been mostly or totally replaced by a secondary assemblage (see text for the details).



Picrites are porphyric with phenocrysts of olivine and, occasionally, clinopyroxene and Cr-spinel (Figures 3B and 4A,B). Phenocrysts of olivine range from 2 to 20 mm in size, euhedral and rounded in shape, moderately serpentinized, and host euhedral rounded inclusions of Cr-spinel. These Cr-spinel grains also occur as <1 mm crystals outside of olivine in the groundmass and occasionally contain melt inclusions (see Section 4.4). Clinopyroxene phenocrysts are 5 to 20 mm in size and occasionally form glomeruli. The picrite groundmass is composed of small (0.1–0.2 mm) grains of clinopyroxene, acicular hornblende, and phlogopite, set in a chlorite-albite-orthoclase-serpentine-apatite cryptocrystalline aggregate (Figure 4B,C). In some samples, plagioclase and K-Na feldspar are abundant in the groundmass (Figure 4D). Hornblende crystals are occasionally replaced by a mineral with a composition close to  $\text{CaSiO}_3$ , which could be wollastonite, but is more likely xonotlite ( $\text{Ca}_6\text{Si}_6\text{O}_{17}(\text{OH})_2$ ), a low-temperature hydrothermal mineral (Figure 4C), while plagioclase and K-Na feldspar were replaced by albite and pure K-feldspar.

Basalts are typically composed of clinopyroxene phenocrysts (2–30 mm in size), set in micro- and cryptocrystalline groundmass (Figure 4E). In some samples, plagioclase phenocrysts and serpentine pseudomorphs after olivine phenocrysts are also present (Figure 4E,F). The groundmass assemblage is represented by microcrystalline clinopyroxene and sparry grains, consisting of patchy-textured albite and K-feldspar (presumably pseudomorphs after magmatic feldspar), which are set in a cryptocrystalline chlorite + orthoclase aggregate (Figure 4G). In addition to typical porphyric basalts, there are also varieties which compose upper parts of differentiated layers and have aphyric amygdaloidal textures, and those which form inner parts of the layers and are distinguished by well-crystallized texture with rodlike boxy crystals of clinopyroxene set in a fine-grained and trachytoidal feldspar matrix (Figure 4H).

Dunites, sampled from the outcrops, are strongly serpentinized and contain only a few relics of olivine (Figure 5A). Former crystals of olivine had sizes presumably of 1–3 mm, as inferred from magnetite lamellae, which remain unmoved during serpentinization. Accessory minerals are represented by magnetite and occasional Cr-spinel, which is hosted in relics of olivine. In addition, we studied a xenolith (aolith?) of dunite (~5 cm × 3 cm) from a picrite sample (21AK47), where olivine is weakly serpentinized (Figure 5B).

Wehrlites are composed of poikilitic clinopyroxene, which contains euhedral to subhedral olivine, and minor phlogopite (Figure 5C). In some samples, clinopyroxene is markedly abundant and exhibits subhedral to euhedral shapes. One of the samples (21AK56) contains 5%–10% of feldspar, which is represented by plagioclase and K-Na feldspar, and minor hornblende, and is classified as plagio-wehrlite (Figure 5D). Importantly, an intergrowth of hornblende and feldspar, resembling eutectic quartz-feldspar textures in granites, was observed in the interstices of the plagio-wehrlite (Figure 5E). Accessory minerals in all varieties of wehrlites are Cr-spinel, magnetite, and apatite. Most of the wehrlites have been subjected to moderate alteration, with olivine being replaced by serpentine and clinopyroxene by actinolite and chlorite.

Gabbroic rocks (see Discussion for classification details) are composed of subhedral and tabular feldspar, which is represented by albite and pure K-feldspar with minor epidote, as well as rounded pseudomorphs of actinolite after clinopyroxene and minor phlogopite (Figure 5F). Clinopyroxene is totally replaced by actinolite in the same way as in wehrlites. Very small (<50 μm) inclusions of clinopyroxene are found in these pseudomorphs, which may represent either relics of primary clinopyroxene or newly-formed “metasomatic” diopside (Figure 5G) (see Section 4.2.2 for further details). Typical accessory phases are apatite, magnetite, and titanite. Notably, one of the samples (21VK1) is characterized by poikilo-ophitic texture, where plagioclase forms euhedral platy crystals, while clinopyroxene forms subhedral poikilitic grains with plagioclase inclusions (Figure 5H). Due to this principal difference from the rest of gabbroic rocks, we hereinafter refer to this sample as a gabbrodolerite.

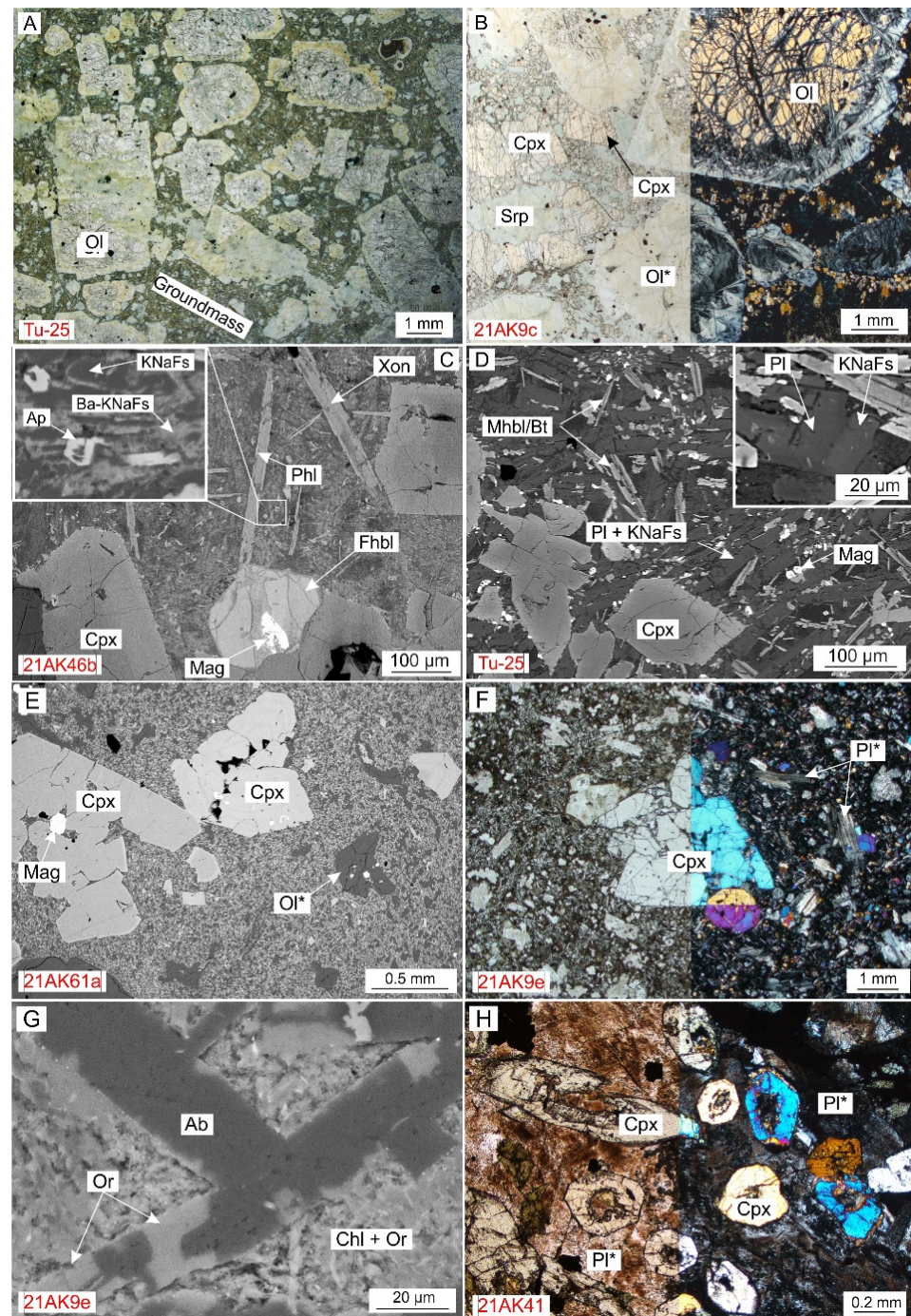


**Figure 4.** Petrographical features of the volcanic rocks. (A) picrite (transmitted light photo); (B) olivine phenocrysts and groundmass clinopyroxene in picrite (transmitted light photo, left side—analyzer out, right—analyzer in); (C) groundmass in picrite (BSE-photo), on the inset—close-scale of the cryptocrystalline aggregate; (D) groundmass in picrite with abundant feldspars (BSE-photo), on the inset—close scale of a zoned feldspar grain; (E) phenocrysts of clinopyroxene and pseudomorphs of serpentine after olivine phenocrysts in basalt (BSE-photo); (F) clinopyroxene and plagioclase phenocrysts in basalt (transmitted light photo, left side—analyzer out, right side—analyzer in); (G) patchy replacement of groundmass feldspar in basalt by albite and orthoclase in a cryptocrystalline aggregate of chlorite and orthoclase (BSE-photo); (H) holocrystalline basalt with rodlike boxy clinopyroxene (transmitted light photo, left side—analyzer out, right side—analyzer in). Hereinafter mineral abbreviations are after [71], in addition, Ba-KNaFs is Ba-rich alkali feldspar. An asterisk (\*) after the mineral symbol means that the mineral has been extensively altered or replaced.

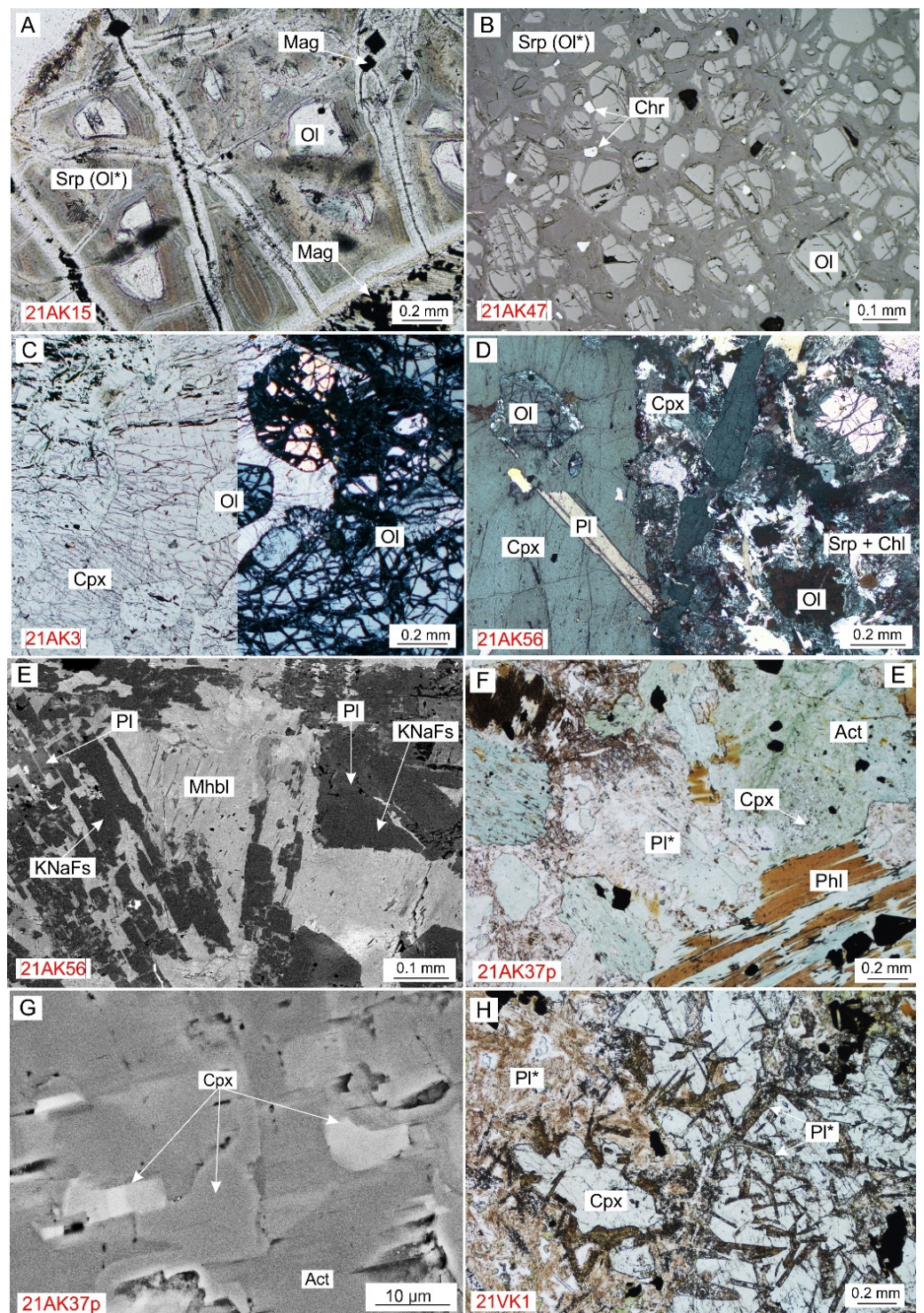


**Figure 5.** Petrographical features of the plutonic rocks. (A) serpentinized dunite (transmitted light photo); (B) partially serpentinized dunite, composing a xenolith in picrite (reflected light photo); (C) wehrlite (transmitted light photo, left side—analyzer out, right side—analyzer in); (D) plagiowehlite (transmitted light photo, analyzer in); (E) intergrowth of magnesiohornblende with K-Na feldspar and plagioclase in an interstice of plagiowehlite (BSE-photo); (F) gabbro (monzogabbro) (transmitted light photo); (G) relics of clinopyroxene in actinolite pseudomorphs, monzogabbro (BSE-photo); (H) clinopyroxene oikocryst with plagioclase inclusions and dolerite (transmitted light photo).

## 4.2. Mineral Chemistry

### 4.2.1. Olivine

Olivine phenocrysts in picrites are largely homogeneous. The Mg# value ( $\text{Mg\#} = \text{Mg} / (\text{Fe} + \text{Mg})$ ) varies from 87 to 90, which is generally lower than those reported previously (88–94) [54,61]. Contents of NiO vary from 0.17 to 0.22 wt.%, CaO between 0.3–0.4 wt.%, and MnO from 0.19–0.24 wt.% (Figure 6). Olivine from dunites, sampled from outcrops, is characterized by Mg# from 89–91. The CaO, MnO, and NiO contents vary in ranges of 0.08–0.14, 0.18–0.19, and 0.21–0.23 wt.%, respectively. Olivine from the dunite autolith within the picrite has a narrow compositional range with Mg#  $88.7 \pm 0.1$ , and concentrations of CaO between 0.37–0.38 wt.% and MnO 0.19–0.20 wt.%. Olivine from wehrlites and plagio-wehrlite has Mg# between 80–81, which is markedly lower than that from picrites and dunites. Contents of CaO, MnO, and NiO in wehrlitic olivine vary in ranges of 0.03–0.06 wt.%, 0.33–0.35 wt.%, and 0.13–0.14 wt.%.

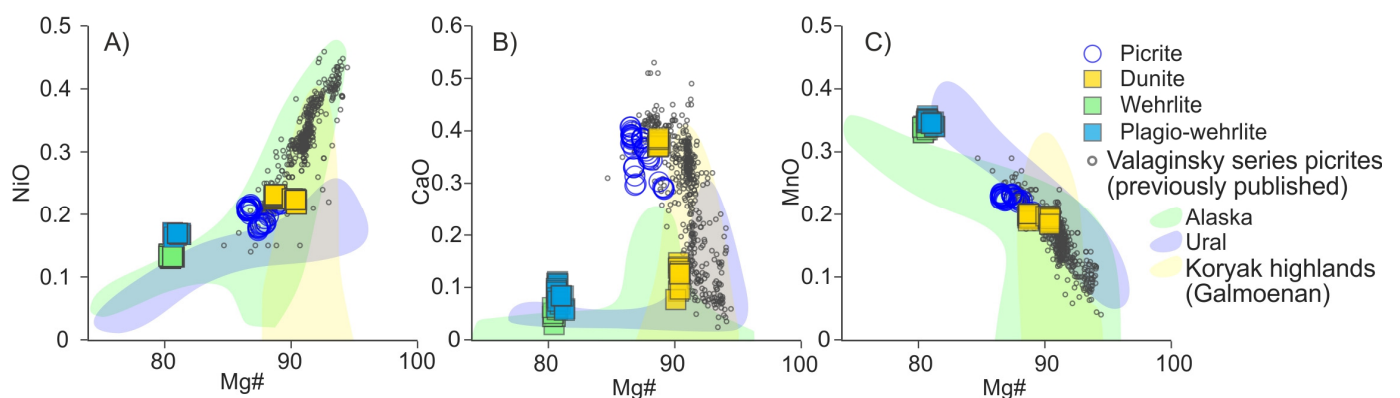


**Figure 6.** Chemical variation plots of olivine compositions from the studied rocks, including previously published data on the Valaginsky series volcanics (both Tumrok and Valaginsky ridge occurrences) [54,61]. (A) Mg#–NiO plot (where  $\text{Mg\#} = \text{Mg} / (\text{Mg} + \text{Fe})$  atomic %); (B) Mg#–CaO plot; (C) Mg#–MnO plot. Compositional fields for Alaska (Kane Peak, Blashke Islands, Slat Chuck, Union Bay) [6], Ural (Nizhniy Tagil, Svetly Bor, Kytlym) [18,48], UA-complexes, and Galmoenan complex [28] are given for comparison.

### 4.2.2. Clinopyroxene

In all samples, clinopyroxene is largely represented by diopside and subordinate high-Ca augite (Figure 7A). Clinopyroxene phenocrysts in picrites are mostly homogeneous, with Mg# ~87,  $\text{Al}_2\text{O}_3$ —1.5–2.0 wt.%,  $\text{Cr}_2\text{O}_3$ —0.5–0.7 wt.%, and  $\text{TiO}_2$ —0.15–0.20 wt.% (Figure 7B–E). Thin rims on clinopyroxene phenocrysts are less magnesian (Mg# 70–75), almost free of  $\text{Cr}_2\text{O}_3$ , enriched in  $\text{Al}_2\text{O}_3$  (5–6 wt.%) and  $\text{TiO}_2$  (0.7–0.8 wt.%) (Figure 8A). Groundmass crystals of clinopyroxene gradually zoned. Inner zones are characterized by Mg# 85–87,  $\text{Cr}_2\text{O}_3$ —0.7–0.9 wt.%,  $\text{Al}_2\text{O}_3$ —1.5–2.0 wt.%, and  $\text{TiO}_2$  below 0.3 wt.%. Outer zones have Mg# 70–75 with one grain having Mg# 65, are virtually free of  $\text{Cr}_2\text{O}_3$ , while contents of  $\text{Al}_2\text{O}_3$  and  $\text{TiO}_2$  approach 7.0–7.5 wt.% and from below the detection limit to 1 wt.%, respectively (Figure 8B).

Clinopyroxene phenocrysts in porphyric basalts are represented by two populations. The first one is two-zoned grains with high-Mg, chromian, low-Al, and low-Ti cores, resembling that of phenocrysts in picrites (Figure 8C). The second one is grains with oscillatory zoning, which is characterized by saw-like chemical profiles with general core-to-edge decrease of Mg# (from 75–80 to 70–75),  $\text{Cr}_2\text{O}_3$  (from 0.4–0.7 in cores to <0.1 in rims), increase of  $\text{Al}_2\text{O}_3$  (from 2.5–3.5 wt.% to 4.5–5.5 wt.%), and  $\text{TiO}_2$  (0.2–0.4 wt.% to 0.5–0.8 wt.%) (Figure 8D). Boxy clinopyroxene from the well-crystallized basalts is also zoned. Inner zones have Mg# 80–84,  $\text{Cr}_2\text{O}_3$ —0.5–0.7 wt.%,  $\text{Al}_2\text{O}_3$ —2–3 wt.%, and  $\text{TiO}_2$ —0.2–0.4 wt.%. Rims are characterized by Mg# 70–75,  $\text{Cr}_2\text{O}_3$  below 0.05 wt.%,  $\text{Al}_2\text{O}_3$ —3–4 wt.%,  $\text{TiO}_2$ —0.7–0.8 wt.%.

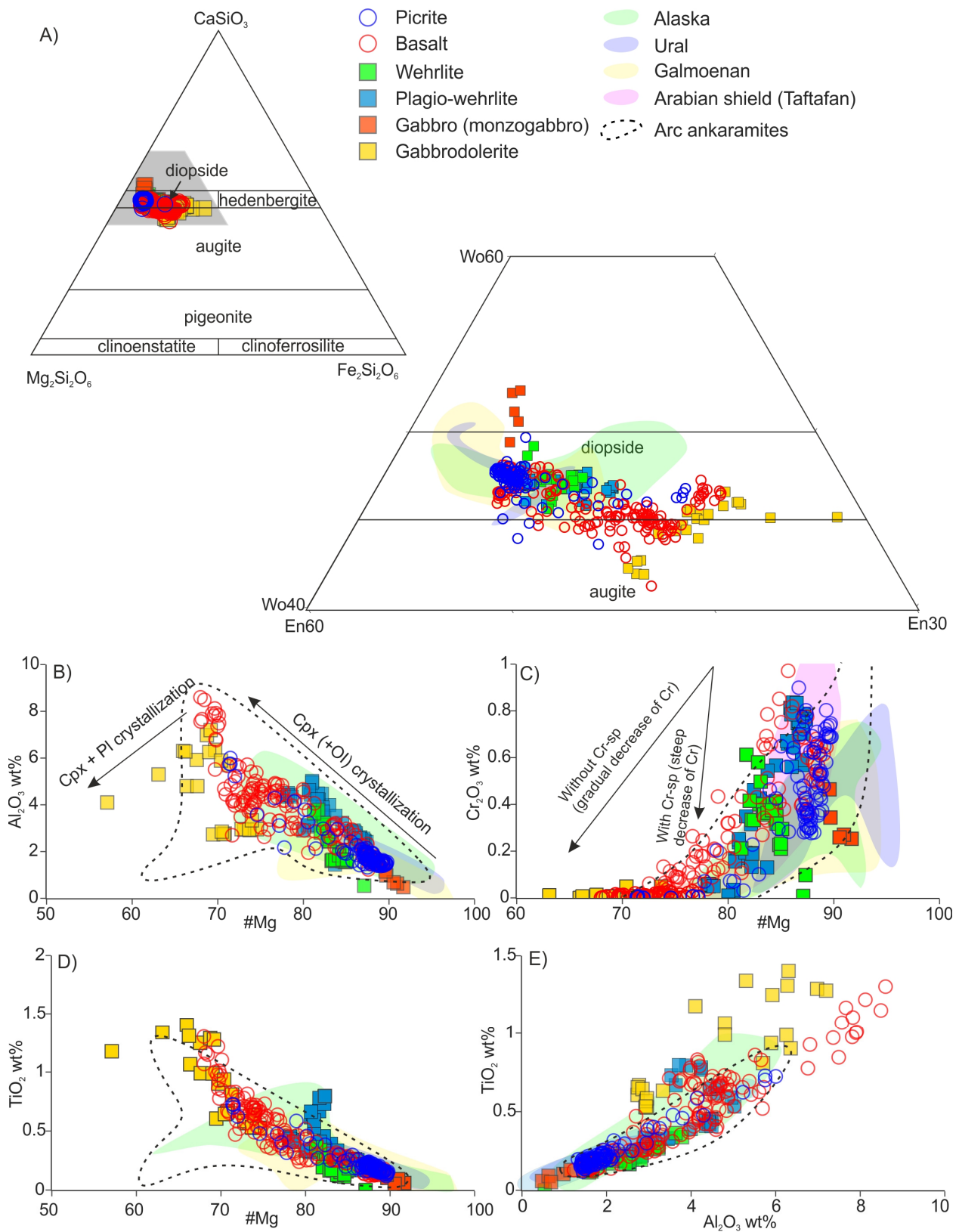


**Figure 7.** Chemical variation plots of clinopyroxene from the studied rocks. **(A)** Triangle En-Wo-Fs plot [72] with a close-scaled sector, shaded on the left diagram. **(B)** Mg#— $\text{Al}_2\text{O}_3$  plot; **(C)** Mg#— $\text{Cr}_2\text{O}_3$  plot; **(D)** Mg#— $\text{TiO}_2$  plot; **(E)**  $\text{Al}_2\text{O}_3$ — $\text{TiO}_2$  plot. Data sources for compositional fields for the Alaskan, Uralian, and Galmoenan complexes are as in Figure 6. Fields for the Taftafan UA-complex (Arabian shield) are based on data from [35]. Fields for arc ankaramites are after [73–77].

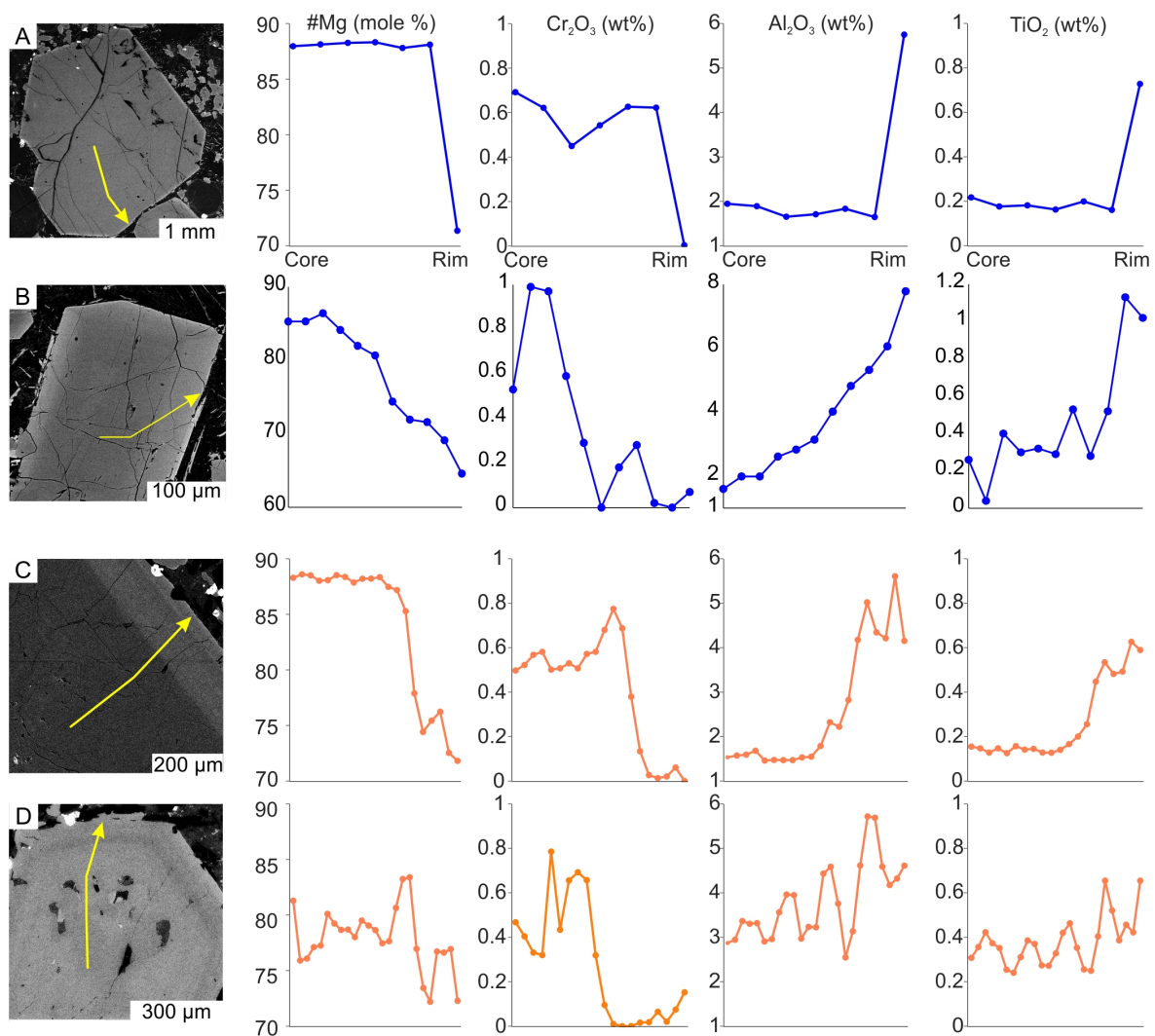


**Figure 8.** Chemical zoning of clinopyroxene grains. (A) Phenocryst, picrite; (B) groundmass grain, picrite; (C) basalt, two-zoned phenocryst; (D) basalt, phenocryst with oscillatory zoning. Images are BSE-photos, and yellow arrows outline core-to-rim microprobe profiles given to the right from the images.

Clinopyroxene grains in plagioclase-free wehrlites are largely homogeneous, yet some unsystematic variations were observed. Mg# varies from 81–85,  $\text{Al}_2\text{O}_3$ —1.5–4.0 wt.%, and  $\text{TiO}_2$ —0.1–0.4 wt.% (Figure 7B–E). Clinopyroxene in plagioclase-wehrlites can be either homogeneous or have two zones. In the latter case, the core is characterized by Mg# 86–87,  $\text{Cr}_2\text{O}_3$ —0.6–0.8,  $\text{Al}_2\text{O}_3$ —2–3 wt.%, and  $\text{TiO}_2$ —0.2–0.25 wt.%, while the rim has Mg# 81–84,  $\text{Cr}_2\text{O}_3$ —0.1–0.2 wt.%,  $\text{Al}_2\text{O}_3$ —0.4–0.5 wt.%, and  $\text{TiO}_2$ —0.5–0.8 wt.%.

Clinopyroxene in actinolite pseudomorphs from gabbros has high-Mg# (89–91), and contains low  $\text{TiO}_2$  (<0.1 wt.%), moderate  $\text{Cr}_2\text{O}_3$  (0.2–0.4 wt.%), and low  $\text{Al}_2\text{O}_3$  (<1 wt.%) (Figure 7B–E). Such compositional features may be explained in two ways. The first is that these are relics of primary clinopyroxene, which underwent re-equilibration with actinolite, and partitioning of Fe and Al to the latter. The second is that this clinopyroxene is secondary, co-genetic with actinolite, and was formed during late fluid-driven processes [78,79].

Clinopyroxene in the dolerite sample has the lowest Mg# compared to other rocks studied (63–65), elevated contents of  $\text{Al}_2\text{O}_3$  (2.0–6.5 wt.%), and  $\text{TiO}_2$  (up to 1.4 wt.%), while  $\text{Cr}_2\text{O}_3$  content does not exceed 0.05 wt.% (Figure 7B–E). Importantly,  $\text{Al}_2\text{O}_3$  contents in clinopyroxene from dolerites are generally lower than those in clinopyroxenes of the same Mg# (Figure 7B).

### 4.2.3. Cr-Spinel

Cr-spinel in picrites is magnesiochromite (Mg# 50–75) and, more commonly, chromite (Mg# 35–50). Cr# value ( $\text{Cr\#} = \text{Cr}/(\text{Cr} + \text{Al})$ ) varies from 65 to 90 with a weak negative correlation with Mg# (Figure 9A). Compositional ranges for Cr-spinel from picritic rocks overlap with those previously obtained for picrites of the Valaginsky series [54,61]. The dunite xenolith from picrite contains magnesiochromite with a relatively narrow compositional range, overlapping with picrites. Cr-spinel from wehrlites and plagio-wehrlite is chromian magnetite, with some analyses corresponding to chromite ( $\text{Cr}/\text{Fe}^{3+}$  cations > 1) (Figure 9B,C). In general, Cr-spinel from the studied rocks forms an oxidizing chemical trend from magnesiochromite in more primitive rocks to chromian magnetite in more evolved (wehrlites) (Figure 9B,C). In addition, a sub-vertical trend of picritic chromite on the Al-Cr-Fe plot (Figure 9C) reflects depletion of the evolving melt in Cr and fractionation of olivine, which makes the melt more Fe- and Al-rich.  $\text{TiO}_2$  and  $\text{Al}_2\text{O}_3$  contents in studied Cr-spinel are moderately low (less than 1 and 15 wt.%, respectively) and are typical of those for the Cr-spinel of arc settings [80] (Figure 9D).

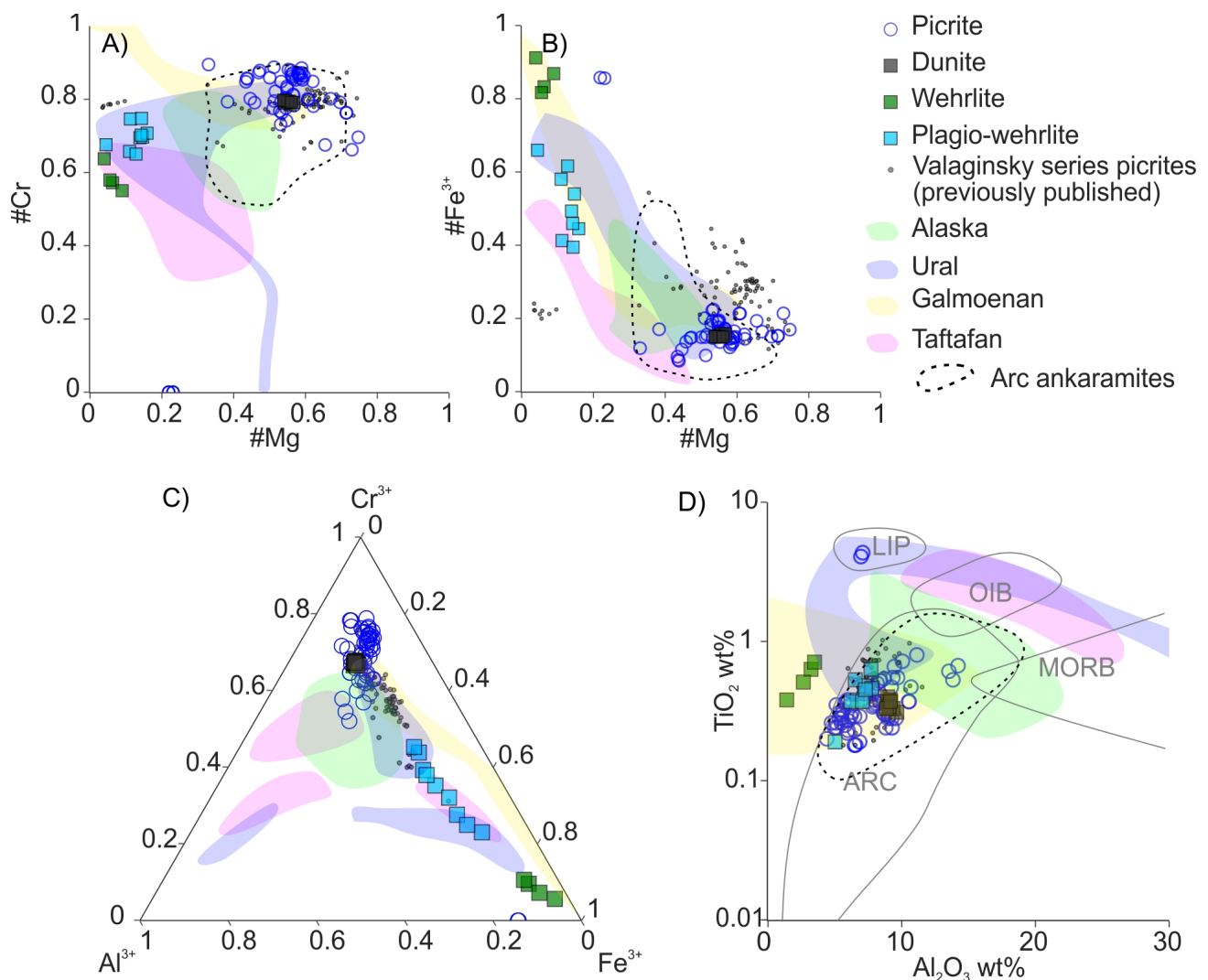


**Figure 9.** Chemical variation plots of Cr-spinel. (A) Mg#–Cr#, where Cr# is  $\text{Cr}/(\text{Cr} + \text{Al})$  atomic %; (B) Mg#–Fe<sup>3+</sup>#, where Fe<sup>3+</sup># is  $\text{Fe}^{3+}/(\text{Fe}^{3+} + \text{Al} + \text{Cr})$  atomic %; (C) Al<sup>3+</sup>–Cr<sup>3+</sup>–Fe<sup>3+</sup> triangle plot; (D) Al<sub>2</sub>O<sub>3</sub>–TiO<sub>2</sub> plot with the fields typical for certain tectonic environments (ARC—arc settings, MORB—mid ocean ridge basalts, OIB—oceanic island basalts, LIP—large igneous provinces) from [80]. Data sources for comparison of the UA-complexes worldwide are as in Figure 7. Fields for arc ankaramites are after [73,81,82].

### 4.3. Rock Chemistry

#### 4.3.1. Major Components

The studied rocks cover a broad range in terms of major element compositions (Table 2). Picrites are high-magnesian (MgO from 23–33 wt.%) and contain low abundances of SiO<sub>2</sub> (39–44 wt.%), Al<sub>2</sub>O<sub>3</sub> (3–7 wt.%), and CaO (3–9 wt.%) (Figure 10A–C). Concentrations of alkalis in picrites vary from 0.1–1.0 wt.% Na<sub>2</sub>O and below detection limit to 2.0 wt.% K<sub>2</sub>O (Figure 10D,E). The CaO/Al<sub>2</sub>O<sub>3</sub> ratio for the picrites is higher than 1 in most of the samples analyzed (Figure 10F). Compositional ranges of picrites are characterized by a reverse correlation between MgO and other oxides with the trend striking to the composition of pure olivine on the MgO axis (Figure 10A–C). Basalts are characterized by SiO<sub>2</sub> content from 47–51 wt.%, MgO—6–13 wt.%, Al<sub>2</sub>O<sub>3</sub>—11–16 wt.%, and CaO from 8.5–11 wt.% (Figure 10A–C). Variations of Na<sub>2</sub>O and K<sub>2</sub>O are unsystematic and quite broad: 0.5–4.5 wt.% and 2–7 wt.%, respectively (Figure 10D,E). The CaO/Al<sub>2</sub>O<sub>3</sub> ratio for the basalts varies from 0.59–1.00 wt.% (Figure 10F). Contents of SiO<sub>2</sub> and Al<sub>2</sub>O<sub>3</sub> are negatively correlated with MgO, while the MgO–CaO trend is positive (Figure 10A–C).

**Table 2.** Chemical composition of the selected samples.

Sample	AK-9c	AK-58	AK-9e	AK-61a	AK-41a	AK-15a	AK-3	AK-34	AK-56	AK-37p	AK-37s	BK-1a
Rock	P	P	B	B	B	Du	W	W	PIW	G(M)	G(M)	Do
SiO <sub>2</sub>	39.32	43.00	50.87	47.85	48.48	34.39	46.61	43.98	43.66	43.78	52.31	49.17
TiO <sub>2</sub>	0.17	0.21	0.53	0.52	0.63	0.04	0.16	0.14	0.19	0.43	0.70	0.70
Al <sub>2</sub> O <sub>3</sub>	3.39	4.28	15.59	10.82	14.08	0.54	2.36	2.26	6.78	8.95	15.47	15.14
FeO	10.24	9.62	7.98	9.70	9.44	9.12	9.67	10.54	11.30	13.36	9.28	8.97
MnO	0.19	0.17	0.14	0.18	0.16	0.19	0.19	0.21	0.20	0.17	0.09	0.14
MgO	31.73	26.62	6.69	12.33	5.97	40.01	23.39	27.09	25.42	16.76	4.82	5.56
CaO	4.80	7.08	9.24	10.92	11.06	0.46	13.88	10.22	5.95	9.58	8.29	10.07
Na <sub>2</sub> O	0.80	<0.1	3.41	1.58	0.78	<0.1	0.33	0.34	0.45	0.85	3.35	0.57
K <sub>2</sub> O	0.16	0.12	2.11	2.05	5.99	0.18	0.48	0.24	2.11	1.86	3.58	6.12
P <sub>2</sub> O <sub>5</sub>	0.11	0.14	0.30	0.26	0.46	0.02	0.04	0.03	0.24	0.40	0.41	0.45
L.O.I.	8.96	8.62	3.00	3.66	2.78	14.95	2.79	4.80	3.53	3.64	1.49	2.96
Total	99.87	99.87	99.87	99.87	99.84	99.90	99.89	99.86	99.83	99.78	99.80	99.85
V	23.39	74.79	276.04	235.06	321.17	2.71	63.89	22.89	96.00	289.10	348.27	322.15
Cr	2572	2036	122	592	112	3503	1340	1899	1366	1018	67	8
Co	97.74	85.66	27.05	44.94	29.61	108.87	80.77	104.71	75.97	72.34	25.58	24.88
Ni	774.0	836.3	72.2	185.7	57.9	1228.7	332.2	520.9	648.4	320.3	44.6	29.7
Cu	23.62	46.14	95.80	94.04	112.67	6.98	36.07	29.77	34.55	117.18	29.07	60.44
Zn	64.78	212.88	50.67	164.29	95.93	62.92	29.20	56.38	94.85	89.45	89.60	74.24
Rb	9.15	12.83	25.99	32.09	51.29	3.07	9.65	4.96	36.04	40.80	43.37	52.84
Sr	47.11	51.98	417.27	243.51	459.02	14.93	42.35	20.80	93.95	151.73	680.38	454.89
Y	3.41	5.23	12.11	12.12	14.30	0.61	3.22	3.12	6.80	8.76	15.73	16.10
Zr	4.75	4.37	18.82	33.60	19.62	0.20 *	3.01	0.80 *	6.93	14.76	43.56	27.38
Nb	0.06 *	0.08 *	0.37 *	0.47 *	0.39 *	0.03 *	0.10 *	0.03 *	0.08 *	0.24 *	0.70 *	0.52 *
Mo	0.30	0.41	0.31	0.57	0.50	0.06	0.23	0.26	0.25	0.64	0.36	0.42
Cs	0.66	2.32	0.12	0.13	0.10	0.07	0.32	0.17	0.96	0.70	0.27	0.13
Ba	1.57 *	18.43	533.76	232.78	599.73	8.20	26.55	15.95	154.59	126.11	982.12	567.83
La	0.45 *	0.94 *	2.43	2.31	3.80	0.16 *	0.39 *	0.16 *	1.22	1.57	4.26	4.42
Ce	1.20 *	2.64	5.91	6.10	9.69	0.40 *	1.07 *	0.57 *	3.30	3.94	10.68	11.42
Pr	0.19 *	0.43	0.87	0.96	1.51	0.05 *	0.18 *	0.11 *	0.52	0.60	1.60	1.72
Nd	1.06 *	2.17	4.45	4.63	7.20	0.22 *	0.92 *	0.69 *	2.63	3.16	7.52	7.89
Sm	0.36 *	0.68 *	1.46	1.49	2.17	0.06 *	0.33 *	0.30 *	0.84	1.00	2.11	2.30
Eu	0.14 *	0.25	0.52	0.53	0.74	0.02 *	0.13 *	0.13 *	0.29	0.32	0.75	0.81
Gd	0.49	0.79	1.67	1.77	2.33	0.08	0.46	0.49	1.00	1.31	2.28	2.46
Tb	0.08	0.13	0.30	0.31	0.40	0.02 *	0.08	0.09	0.17	0.24	0.39	0.42
Dy	0.57	0.83	1.95	2.00	2.49	0.10	0.52	0.58	1.05	1.53	2.43	2.61
Ho	0.12	0.18	0.42	0.43	0.50	0.02	0.11	0.11	0.22	0.33	0.53	0.56
Er	0.35	0.49	1.27	1.29	1.41	0.06 *	0.32	0.31	0.66	0.91	1.55	1.61
Tm	0.05 *	0.08 *	0.19	0.20	0.21	0.01 *	0.05 *	0.05 *	0.10 *	0.13	0.25	0.24
Yb	0.31	0.50	1.22	1.22	1.31	0.07 *	0.28	0.31	0.65	0.88	1.62	1.55
Lu	0.06	0.07	0.18	0.18	0.18	0.01 *	0.04	0.05	0.09	0.14	0.23	0.21
Hf	0.17 *	0.19 *	0.66	0.89	0.70 *	0.02 *	0.12 *	0.01 *	0.25 *	0.44 *	1.27	0.89



Table 2. Cont.

Sample	AK-9c	AK-58	AK-9e	AK-61a	AK-41a	AK-15a	AK-3	AK-34	AK-56	AK-37p	AK-37s	BK-1a
Rock	P	P	B	B	B	Du	W	W	PIW	G(M)	G(M)	Do
Ta	0.03 *	0.01 *	0.05 *	0.05 *	0.05 *	0.02 *	0.05 *	0.02 *	0.004 *	0.01 *	0.12	0.02 *
W	0.03	0.12	0.01	4.51	2.01	0.44	0.49	0.04	0.15	0.75	1.13	2.81
Tl	0.06	0.06	0.21	0.26	0.19	0.005	0.06	0.04	0.11	0.12	0.08	0.17
Pb	1.32	10.36	3.57	25.73	3.60	0.15	1.54	0.78	0.50	6.87	2.38	2.47
Th	0.04	0.11	0.22	0.24	0.37	0.02	0.04	0.02	0.12	0.18	0.53	0.52
U	0.04 *	0.06 *	0.15 *	0.24	0.26	0.01 *	0.06	0.04 *	0.12 *	0.12 *	0.38	0.33

Rock name abbreviations: P(A)—picrite, B—basalt, Du—dunite, W—wehrlite, PIW—plagio-wehrlite, G(M)—gabbro (monzogabbro), Do (dolerite). Oxide concentrations are in weight %, element concentrations are in ppm. Values marked by an asterisk (\*) are below detection limits, reported in [70]. However, since the paper, which the analysis protocol refers to [70], was published, the method has been improved, so these analyses should be treated as semi-quantitative.

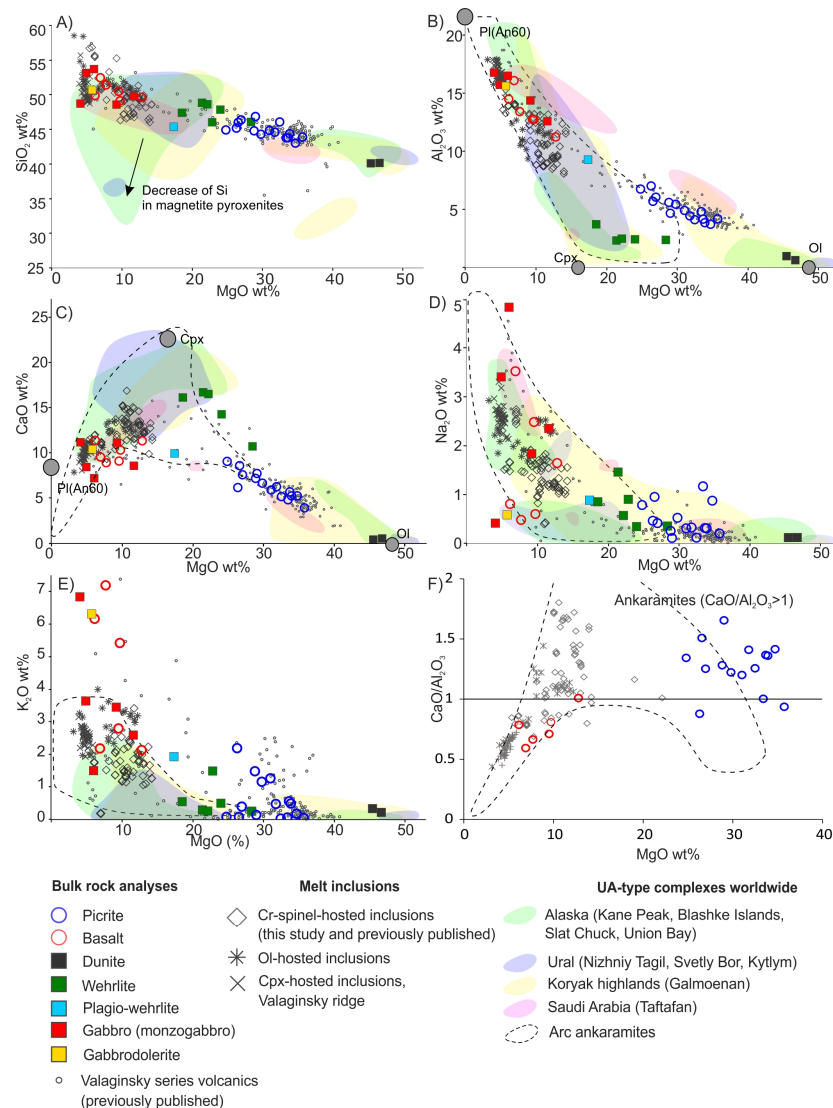
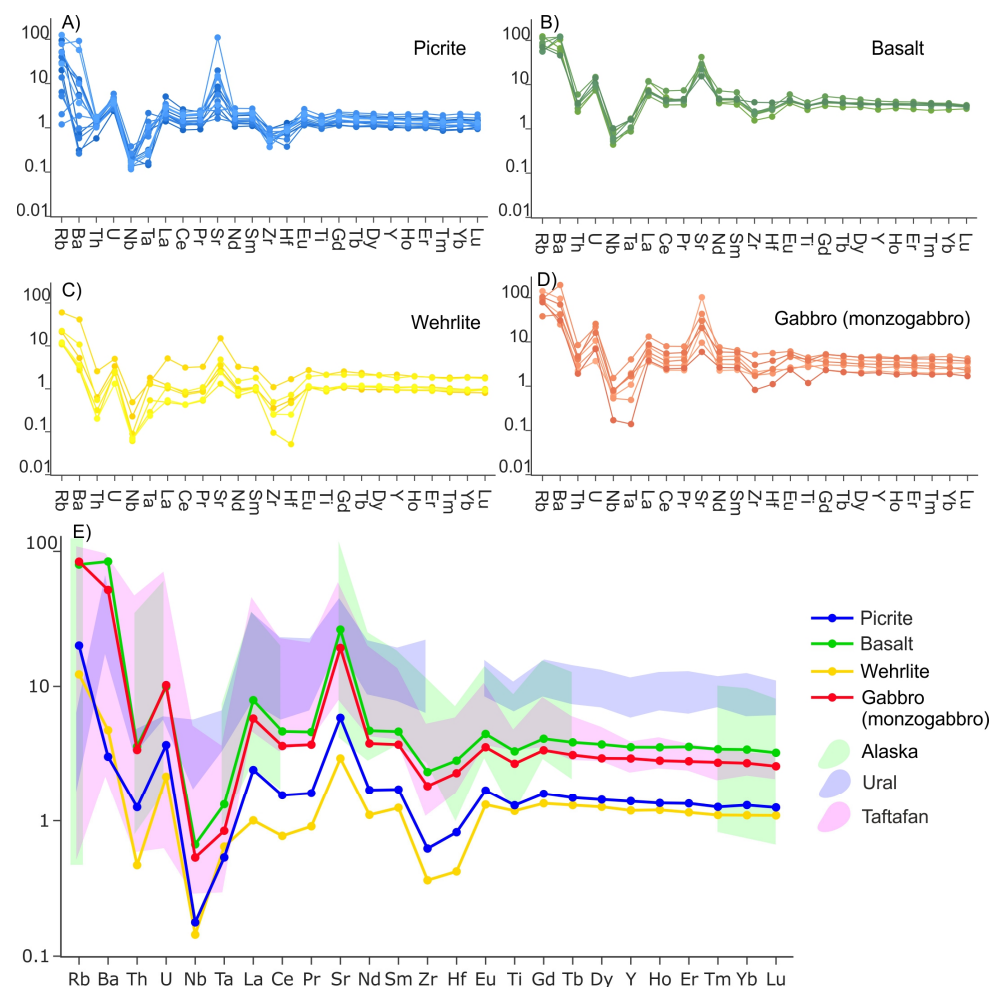


Figure 10. Major component variation plots of the bulk-rock and homogenized melt inclusions' compositions. (A) MgO-SiO<sub>2</sub> plot; (B) MgO-Al<sub>2</sub>O<sub>3</sub> plot with points of average olivine and clinopyroxene compositions and plagioclase (An<sub>60</sub>) from the studied rocks; (C) MgO-CaO plot with the points of mineral compositions the same as on (B); (D) MgO-Na<sub>2</sub>O plot; (E) MgO-K<sub>2</sub>O plot; (F) MgO-CaO/Al<sub>2</sub>O<sub>3</sub> plot: only for the volcanics. Data for melt inclusions are from this study and [54,61]. Data sources for comparison of the UA-complexes worldwide are as in Figure 7. Fields for arc ankaramites are after [74,75,77,82–87].

Dunites have the highest MgO (around 40 wt.%), contain between 34–35 wt.% of SiO<sub>2</sub>, and are deficient in other components, plotting near the “olivine” endmember of the picrite trend (Figure 10A–E). Wehrlites (except a plagiowehlite sample) are rich in MgO (18–27 wt.%) and CaO (10–17 wt.%), contain moderate abundances of SiO<sub>2</sub> (34–35 wt.%), and are deficient of Al<sub>2</sub>O<sub>3</sub> (2–4 wt.%). Contents of SiO<sub>2</sub>, CaO, and Na<sub>2</sub>O in wehrlites are negatively correlated with MgO (Figure 10A–E). The compositions of gabbros vary broadly with SiO<sub>2</sub> content between 44–53 wt.%, MgO content between 4–12 wt.%, CaO—7–11 wt.%, Al<sub>2</sub>O<sub>3</sub>—9–17 wt.%. Similar to the basalts, the abundances of alkalis are generally high and extremely variable: 0.5–5.0 wt.% of Na<sub>2</sub>O and 1.5–7.0 wt.% of K<sub>2</sub>O. Characteristics for the gabbros are negative SiO<sub>2</sub>-MgO, Al<sub>2</sub>O<sub>3</sub>-MgO, and Na<sub>2</sub>O-MgO correlations (Figure 10A–E).

#### 4.3.2. Trace Elements

The studied rocks are characterized by generally uniform patterns of the incompatible lithophile trace elements, but are different in their absolute concentrations. For all the samples analyzed, primitive mantle (PM) normalized (after [88]) trace element patterns have typical supra-subduction signatures, which have negative anomalies of Nb and Ta and positive large ion lithophile element (LILE) (Rb, Ba, and Sr) and U anomalies. In addition, most of the compositions possess more or less pronounced negative anomalies in Zr and Hf (Figure 11A–D). Generally, PM-normalized patterns of the wehrlites overlap with those of the picrites, and patterns of the basalts are almost identical to those of gabbros (Figure 11E).



**Figure 11.** Trace element PM-normalized [88] spider-diagrams for the bulk-rock compositions. (A) Picrites (ankaramites); (B) basalts; (C) wehrlites; (D) gabbros (monzogabbros); (E) averaged compositions of the rock varieties compared to compositions of the rocks of UA-complexes worldwide. Sources of data for the comparison are in Figure 7.

Absolute concentrations of selected incompatible trace elements are negatively correlated with MgO content and positively with each other (Figure 12A–D). Concentrations of relatively mobile Sr show quite good correlation with Ce (Figure 12B), while those of less mobile Yb and Th are perfectly correlated with Ce and show a single trend for all the rocks studied (Figure 12C,D). Concentrations of the compatible trace elements (Ni and Cr) were also considered. Ni is the highest in picrites and dunites (500–1200 ppm) and decreases with decreasing MgO to <50 ppm in the least magnesian basalts and gabbros (Figure 12E). Contents of Cr are the highest in dunites (~3000 ppm) and show a linear decrease, with decreasing MgO to 50–1000 ppm in gabbros and basalts (Figure 12F).

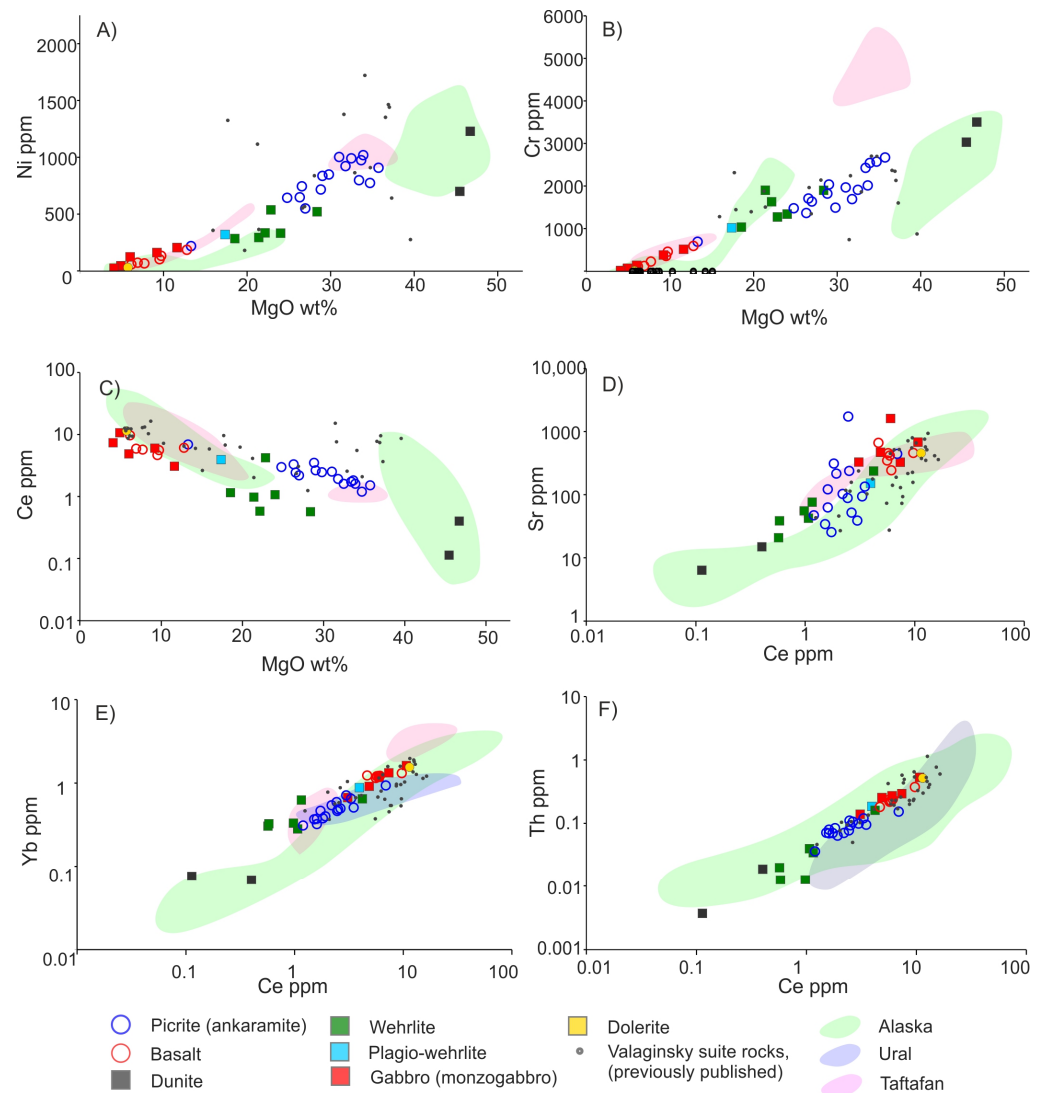


**Figure 12.** Chemical variation plots of trace elements. (A) MgO–Ce plot; (B) Ce–Sr plot; (C) Ce–Yb plot; (D) Ce–Th plot; (E) MgO–Ni plot; (F) MgO–Cr plot. Sources of data for the comparison are in Figure 7.

#### 4.4. Chromite-Hosted Inclusions

Multiphase silicate inclusions occur in Cr-spinel grains, most of which are enclosed by olivine phenocrysts of picrites. The inclusions are round or slightly oval in shape, range in size from 5 to 60  $\mu\text{m}$  in diameter, and are composed predominantly of silicate glass with crystals of clinopyroxene and subordinate hornblende (Figure 13). Bubbles are present in the majority of the inclusions. Based on their occurrence and phase assemblage, the inclusions are primary and represent entrapped melt, which underwent partial post-entrapment crystallization [89].

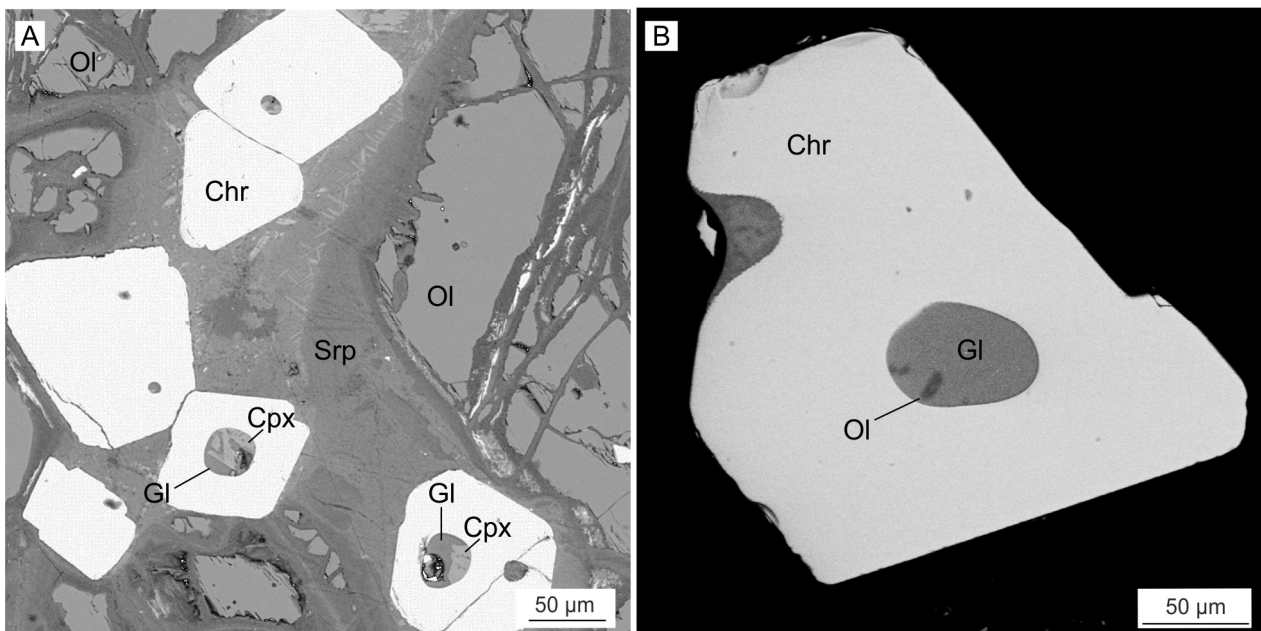


**Figure 13.** BSE photos of the chromite-hosted inclusions. (A) Grains with the melt inclusions, which used to be included in olivine and now are located in a serpentinized fracture; (B) heated up to 1250 °C and quenched melt inclusion.

Upon heating at 1250 °C and quenching, the inclusions turn into a homogenous glass with occasional small crystals of olivine (Figure 13B) and occasional shrinkage bubbles. The compositions of the obtained glasses are close to the compositions of the basalts and exhibit overlap (Figure 10). Compositions with the highest MgO (13–14 wt.%) have SiO<sub>2</sub> contents between 48–50 wt.%, Al<sub>2</sub>O<sub>3</sub> between 8–10 wt.%, and CaO—12–14 wt.% (Figure 10A–C). Concentrations of Na<sub>2</sub>O and K<sub>2</sub>O in the heated inclusion glasses are 1.0–1.3 wt.% and 1.8–2.2 wt.%, respectively (Figure 10D,E). The CaO/Al<sub>2</sub>O<sub>3</sub> ratio ranges from 0.8 to 1.8 and is above 1 in most of the inclusions.

## 5. Discussion

### 5.1. Co-Magmatism of the Studied Rocks

Based on the spatial proximity, mineral compositions, and age determinations [58,59,64] of the studied volcanic and plutonic rocks, it has been supposed that these rocks are genetically related [58,59]. Our data, showing that chemical and mineralogical features of the volcanic and plutonic rocks are generally the same, provide further support for this genetic link. Compositions of clinopyroxene, which is a common rock-forming mineral for all rock varieties, except dunites, form uniform trends with fully overlapping fields between clinopyroxene from volcanic and plutonic rocks (Figure 7). The same differentiation trends and overlapping fields for volcanic and plutonic rocks are formed by variations of bulk major and trace element concentrations (Figures 10 and 12). Finally, PM-normalized systematics of incompatible trace elements are identical for picrites and wehrlites, as well as for basalts and gabbroic rocks, respectively (Figure 11).

We propose that the studied volcanic (and subvolcanic) rocks of the Valaginsky series and plutonic rocks of the Andrianovsky pluton are co-magmatic and form a continuous differentiated series of high-magnesian (dunites, picrites) to low-magnesian (basalts, gabbros and dolerites). The fact that the plutonic body is bordered by faults with no intrusive contacts with the host Valaginsky series observed (Figure 1B) [59,63] implies that the intrusive rocks were crystallized at depth and then tectonically uplifted to the same level as the volcanic series. Alternatively, the plutonic assemblage could have been uplifted as a semi-solid diapir, which is reported as typical for ultramafics in UA-complexes [2,14,45].

## 5.2. Classification of the Series

Based on their mineral composition and textures, as well from data from the previous studies [58,59,63], the studied rocks were initially classified as rocks of normal alkalinity: picrites, basalts, dunites, wehrlites, and gabbros. However, many samples contain minerals, such as biotite and K-Na feldspar, and have elevated alkali contents in their bulk composition (Table 1; Figure 10D,E and Figure 14A). Picrites and plagioclase-wehrlites contain zoned grains with a plagioclase core and K-Na feldspar rims, which are considered to be primary magmatic (Figures 4D and 5E). On the other hand, most of the rocks, including all gabbros and basalts, contain major albite and pure orthoclase, which are not primary magmatic [90,91]. Therefore, the contents of  $\text{Na}_2\text{O}$  and  $\text{K}_2\text{O}$  in the studied rocks are not primary features and cannot be used for classification. To elucidate the true alkalinity of the volcanics, geochemical discrimination based on immobile element systematics was applied [92], according to which the picrites and basalts should be classified as sub-alkaline (Figure 14B). A classification of ultramafic volcanic rocks, as suggested by Le Bas (2000) [93], shows that the picrites, which contain  $>18$  wt.%  $\text{MgO}$  and generally  $<1$  wt.% of  $\text{K}_2\text{O} + \text{Na}_2\text{O}$ , should be termed as “komatiites”. However, they do not exhibit spinifex texture, which is a required feature for komatiitic rocks. Therefore, we decided to retain the term “picrites” for these rocks.

As the studied rocks are co-magmatic, their classification can be discussed further based on melt inclusions in minerals of the Valaginsky volcanic series, which includes the studied occurrence. Most of the Cr-spinel-hosted inclusion compositions are basaltic, whereas olivine-hosted inclusions [61] are transitional between basaltic and trachybasaltic (Figure 14A).

The abundance of clinopyroxene in picrites and scarcity of plagioclase phenocrysts in basalts is characteristic of ankaramites [7,74,94,95], a specific high-Ca sub-group of mafic and ultramafic volcanics, which have  $\text{CaO}/\text{Al}_2\text{O}_3 > 1$  and clinopyroxene phenocrysts dominating over olivine phenocrysts [74,81]. The studied picrites and most of the chromite- and olivine-hosted inclusions fulfill the main chemical criterion of ankaramites:  $\text{CaO}/\text{Al}_2\text{O}_3 > 1$  [74,81] (Figures 10F and 15). The compositional field for basalts, gabbros, and clinopyroxene-hosted inclusions originates in the “ankaramitic” field and then transits to “non-ankaramitic” due to differentiation and increase of  $\text{Al}_2\text{O}_3$  (Figures 10F and 15). Furthermore, fields and trends of bulk-rock, clinopyroxene, and chromite compositions largely overlap with those, which is characteristic for arc ankaramites (Figures 7, 9 and 10). Hence, the bulk-rock chemistry clearly points out that the studied rock series is ankaramitic. However, neither picrites or basalts can be classified as *sensu stricto* “ankaramites”—in the former, olivine dominates over clinopyroxene in a phenocryst population, while the  $\text{CaO}/\text{Al}_2\text{O}_3$  ratio of the latter is generally below 1 (except for the 21AK61a sample—the only sample which can be termed “ankaramite”). Therefore, the correct terms for these rocks are “ankaramitic picrites” and “clinopyroxene basalts of the ankaramitic series”.

Rigorous classification of the gabbroic rocks is complicated by their significant replacement by secondary minerals: low-T feldspars and actinolite (Figure 5F,G). This makes chemical classification for these rocks inapplicable, and complicates mineralogical classification. However, as picrites and a plagioclase-wehrlite contain both plagioclase and K-Na feldspar as primary minerals (Figures 4D and 5E), we considered that feldspars in gabbroic rocks used to be represented by both plagioclase and K-Na feldspars as well. This is indirectly supported by the fact that the assemblage, replacing primary feldspar, contains both alkaline (orthoclase and albite) and calcic (scapolite and epidote) secondary minerals. Hence, the gabbroic rocks can be classified as “monzogabbro”.

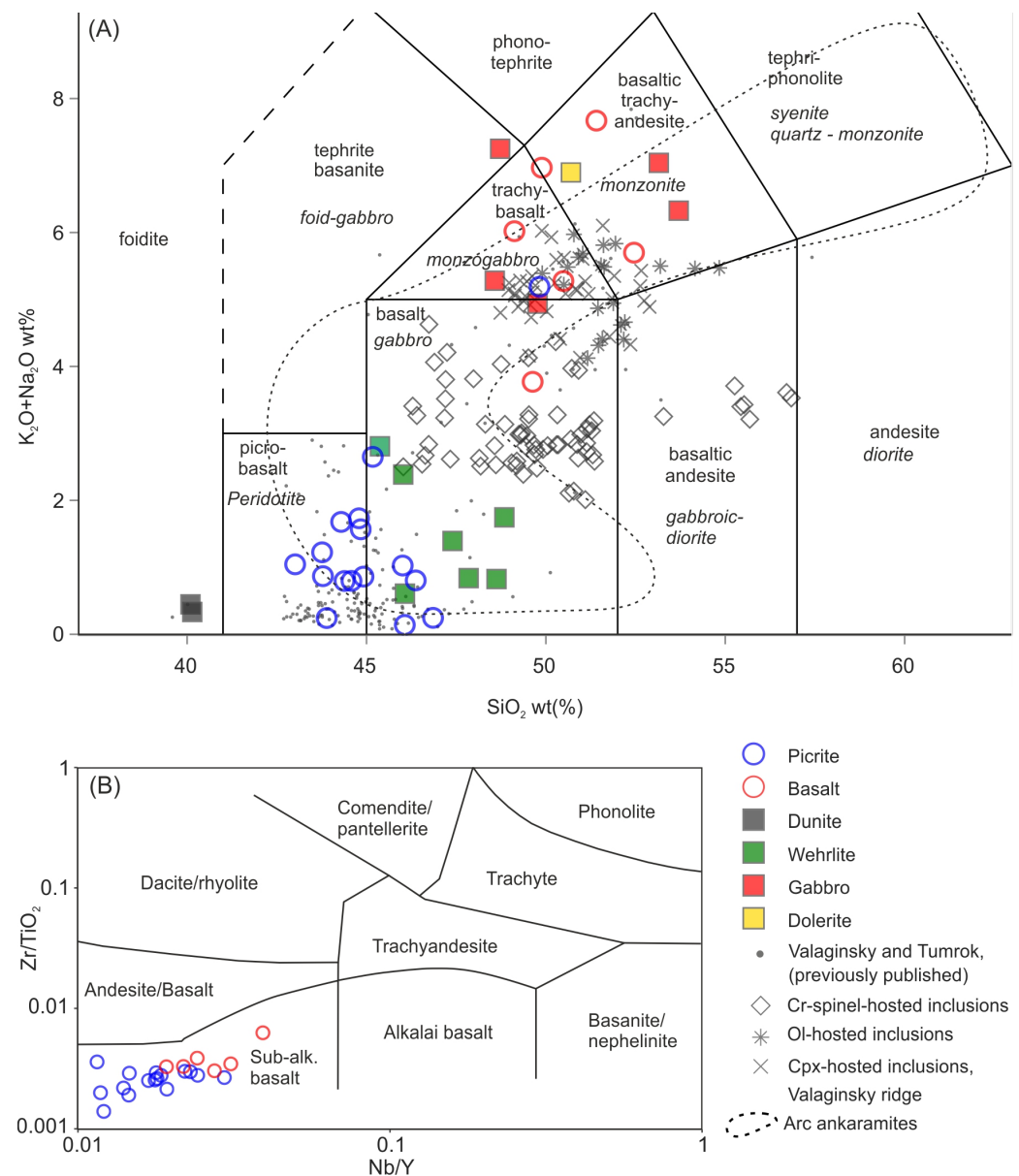


**Figure 14.** Compositions the studied rocks and inclusions on the classification plots. (A) TAS diagram [96] for the volcanic rocks and their plutonic counterparts [97]; (B) Nb/Y-Zr/TiO<sub>2</sub> diagram for volcanic rocks [92]. Data for melt inclusions are from this study and [54,57,61]. Data sources for the fields of arc ankaramites are in Figure 10.

### 5.3. Magmatic Differentiation

A broad variety of rocks, as well as melt inclusion data available, allow for estimation of the parental melt composition and reconstruction of the crystallization sequence. The differentiation path is well illustrated in MgO \* Al<sub>2</sub>O<sub>3</sub>-CaO coordinates [15,19,77] (Figure 15), while the suggested crystallization sequence is given in Figure 16.

The parental melt, which was estimated in previous studies using olivine-hosted melt inclusions [61], contained 19 or 24 wt.% of MgO if calculated using models of Ford et al. (1983) [98] and Sobolev and Slutsky (1984) [99], respectively. The most magnesian chromite-hosted inclusions from Tumrok picrites (this study and [54]), contain 13–14 wt.% MgO, which is significantly lower than that in the calculated primary melt. On the one hand, MgO content in chromite-hosted melt inclusions should be less affected by post-entrapment re-equilibration with the host than in olivine-hosted ones [100] and, therefore, be a better

approximation for the MgO content in the entrapped melt. Moreover, MgO values obtained using numerical algorithms for recalculation of olivine-hosted inclusions [98,99] might be overestimated because the Mg# of olivine depends directly [101,102] on oxidation of the melt and, therefore, an underestimation of the  $f(\text{O}_2)$  chosen for the recalculation may have strongly affected the resulting MgO value. On the other hand, compositions reported in this study were obtained for the inclusions hosted by chromite, that was in equilibrium with  $\text{Fo}_{89-90}$ , while the most primitive olivine of the studied series is  $\text{Fo}_{93-94}$  [54,61]. Therefore, we assume that the actual composition of the initial melt was between 14 and 19 wt.% of MgO, which is consistent with the previous estimations for ankaramitic rocks [75,77] and clinopyroxenites of the Uralian UA-complexes [51].

Differentiation of such a melt begins with Ol + Chr co-crystallization (Figure 16), which forms dunite cumulates and phenocrysts in picrites. Most of the picrites are richer in MgO than the estimated parental melt and contain an excess of olivine (Figure 15). Apparently, picrites were formed from a magmatic mush, containing melt and settling of olivine crystals.

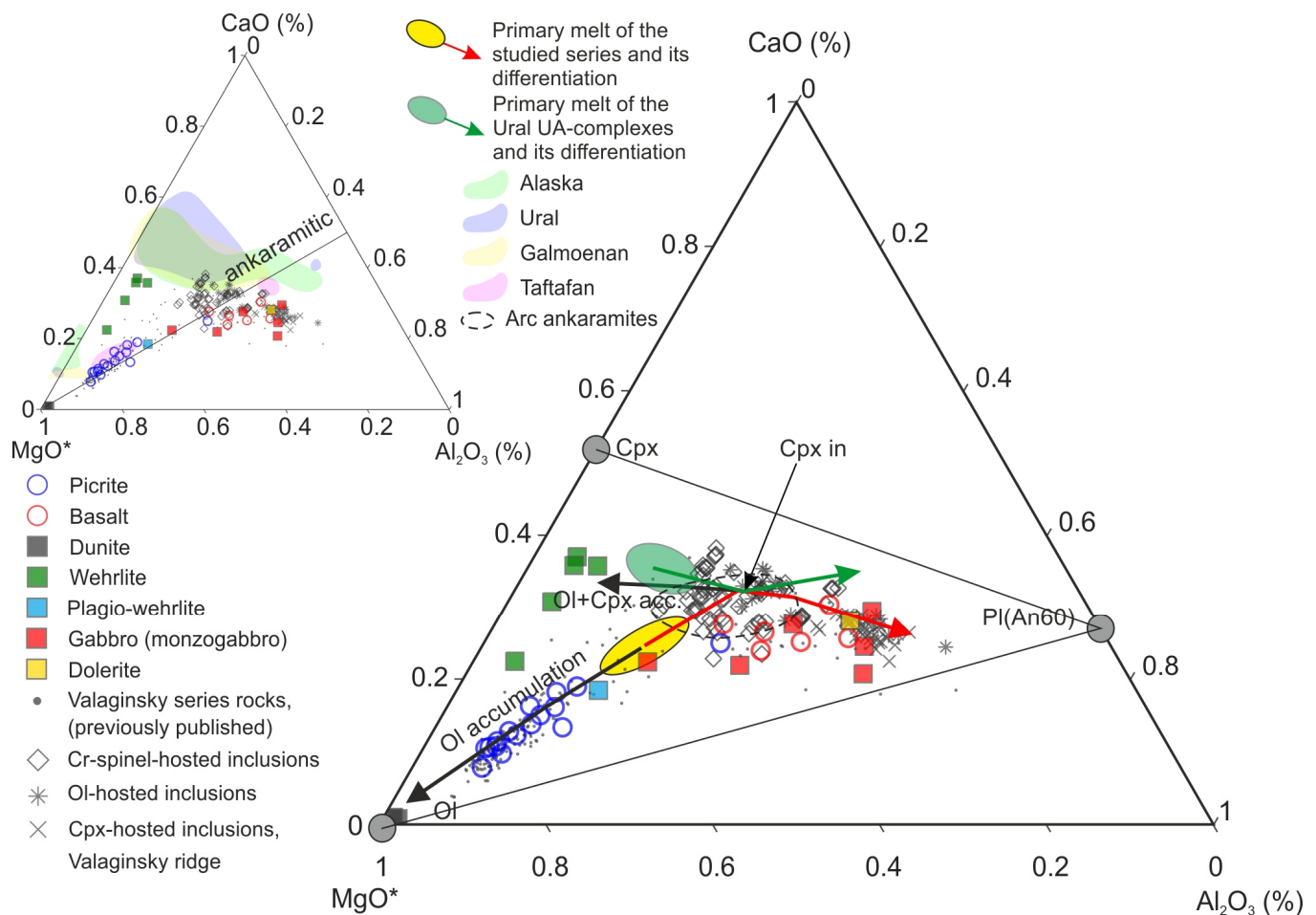


**Figure 15.** Compositions of the studied rocks plotted in MgO\*-CaO-Al<sub>2</sub>O<sub>3</sub> coordinates, where  $\text{MgO}^* = \text{MgO} + 0.55\text{FeO}$  [15,19,77]. Primary melt for our series is estimated as average between compositions of the chromite-hosted melt inclusions and the estimation of Kamenetsky et al. (1995). Primary melt of the Ural UA-complexes and its differentiation trend are from [15,19]. Data for melt inclusions are from this study and [54,61]. Data sources for the fields of the UA-complexes worldwide are as in Figure 10. Data sources for the field of arc ankaramites are from [74,81,103].

The process of olivine crystallization decreases the MgO content and increases all other components in the fractionating melt. At a certain point, clinopyroxene begins to crystallize together with olivine (Figures 15 and 16). During this stage, wehrlites are

formed as cumulative plutonic rocks due to co-accumulation of crystallizing olivine and clinopyroxene or as growth of clinopyroxene in olivine orthocumulates. Clinopyroxene in picrites has two generations (phenocrysts and groundmass grains). It is supposed that homogeneous high-Mg# cores of clinopyroxene phenocrysts (Figure 8A) were formed in a magma chamber, while thin low-Mg# rims formed during magma ascent or in situ growth in surficial or sub-volcanic settings. Growth of the groundmass clinopyroxene (Figure 8B) likely took place during both ascent and in situ crystallization of a picritic body, thus explaining the broad compositional range of these grains. Clinopyroxene phenocrysts in basalts can be divided into large phenocrysts with a high-Mg# homogeneous core (Figure 8C), which crystallized in a slowly cooling magmatic chamber at depths, and smaller ones (Figure 8D), in which oscillatory zoning may reflect their growth during magma ascent under rapidly changing conditions.

Alumina-rich silicates: plagioclase, K-Na feldspar, hornblende and biotite are the latest crystallizing silicates in this series (Figure 16). In volcanic rocks, these minerals do not occur as phenocrysts (except in one sample of plagioclase-clinopyroxene basalt) and are supposed to have crystallized during rapid cooling in surficial or sub-surficial settings. Spatial relationships between feldspar and clinopyroxene in the monzogabbros suggest that clinopyroxene crystallized prior to feldspar. However, the texture of the least magnesian gabbroic rock, classified as gabbrodolerite (Figure 5H), reveals simultaneous crystallization of plagioclase and clinopyroxene and may thus reflect the terminal (eutectic) stage of crystallization. Similar eutectic-like intergrowths of hornblende and feldspar (represented by both plagioclase and K-Na feldspar) were observed in interstices of the plagioclase-wehrlite (Figure 5E) and point to crystallization under higher pressures of H<sub>2</sub>O [104] than in gabbrodolerites. Noteworthy, the fact that decreases in Al<sub>2</sub>O<sub>3</sub> in clinopyroxene were observed only in the marginal rinds of phenocrysts and in poikilitic clinopyroxene from dolerites (Figure 7B,E) suggests that feldspar crystallization took place at the last stage of melt differentiation.

In terms of rock-forming silicates, our data imply that dunites and, to a certain extent, picrites resulted from crystallization and accumulation of olivine only. Wehrlites and the early stages of picrite groundmass crystallization correspond to the olivine-clinopyroxene cotectic. The monzogabbros are products of more or less simultaneous in situ crystallization of plagioclase and clinopyroxene, which apparently finalizes with Pl + KNaFs + Cpx(Hbl) eutectic. This sequence agrees with experimental studies in the Ab(Or)-An-Fo-Di [7,104–107] and represents a good example of a complete differentiation sequence from the olivine liquidus to alkali feldspar crystallization. In addition, the rock assemblage and relationships between the rock-forming minerals are identical to those of other highly-differentiated ankaramitic occurrences [94,108,109], thus implying that the described crystallization sequence can be considered as universal for such magmas.

Accessory minerals (apatite and magnetite) were not found as phenocrysts in volcanic rocks, while their abundance in the plutonic rocks increases with the decreasing of the MgO content, showing that both these minerals crystallized at a relatively late stage (Figure 16). In the groundmass of picrites, magnetite may be euhedral with respect to hornblende, while apatite is only found as needle-like microscopic crystals in the groundmass together with feldspars and secondary minerals. Therefore, we assume that magnetite crystallization slightly preceded crystallization of hornblende, while apatite is one of the latest minerals in the sequence.

During the post-magmatic stage (Figure 16), serpentine formed pseudomorphs after olivine. Albite, orthoclase, muscovite, epidote, and scapolite replaced feldspars. Actinolite and chlorite replaced clinopyroxene and hornblende.



Mineral	Magmatic		Post-magmatic
	Phenocrysts in the volcanics and euhedral grains in the plutonics	Groundmass in the volcanics and interstitial in the plutonics	
Olivine	██████████		
Cr-spinel	██████████		
Clinopyroxene	██████████	██████████	
Plagioclase		██████████	
Hornblende		██████████	
K-Na feldspar		██████████	
Magnetite	██████████		
Biotite/phlogopite		██████████	
Apatite		██████████	
Albite			██████████
Orthoclase			██████████
Actinolite			██████████
Serpentine			██████████
Chlorite			██████████
Scapolite			██████████
Epidote			██████████
Muscovite			██████████

**Figure 16.** Crystallization sequence for the studied complex. Heavy lines refer to the rock-forming minerals (and abundant crystallization), and light lines refer to the minor and accessory minerals (and minor crystallization).

#### 5.4. Comparison to the Ural-Alaskan Complexes

The plutonic assemblage of the Andrianovsky pluton, which includes dunites, wehrlites, gabbroic rocks, is typical of Ural-Alaskan type complexes [6,8,15]. Moreover, the volcanics of the Tumrok range have been supposed to represent close proxies to the volcanic counterparts of the plutonic rocks of the Galmoenan complex, which is a UA-complex with economic PGE mineralization [1]. To investigate whether the studied volcano-plutonic complex can be considered as the UA-type (regardless of its PGE potential) in more detail, we compared its mineralogical and geochemical features with different UA-complexes from localities worldwide. Localities for comparison include plutons of the Ural and Alaskan belts [6,15,18,48], Galmoenan complex of the Koryak highlands [1,24,28], which is the closest UA-complex to the studied occurrence, and Taftafan complex of the Arabian shield [35], which is an example of a Proterozoic UA-complexes.

Our comparison shows that the geochemical and mineral features of the Andrianovsky pluton are very similar to the other UA-complexes. There is almost complete overlap in the  $\text{SiO}_2$ -MgO and  $\text{Na}_2\text{O}$ -MgO variations and significant similarity in  $\text{Al}_2\text{O}_3$ -MgO variations (Figure 10A,B,D). Although CaO contents of the studied complex are slightly lower than that of other UA-complexes, gabbroic rocks overlap with the compositional fields of those from Galmoenan, Alaskan, and Arabian UA-complexes (Figure 10C). In addition, they all have similar  $\text{MgO}^*-\text{CaO}-\text{Al}_2\text{O}_3$  relationships with a characteristic decoupling of olivine + clinopyroxene accumulation and melt differentiation (gabbro + basalts) trends (Figure 15). However, a differentiation trend on this triangle is somewhat different from that suggested by Fershtatter et al. (1999) [15] and Pushkarev (2000) [19] for the Ural belt complexes. These studies implied that the melt composition was close to the olivine-pyroxene cotectic, but decompression during its upwelling resulted in an equilibrium shift, making it saturated with only olivine. In addition, the separation of olivine-rich and olivine-clinopyroxene-rich assemblages likely took place due to dynamic differentiation, as suggested by Murray (1972) [29]. Our data, as well as studies of Kamenetsky et al. (1995) [61] and Batanova et al. (2005) [1], show that the melt composition lay closer to the olivine end-

member and supports that crystallization of only olivine accompanied by minor Cr-spinel was the first stage of the magma's evolution (Figures 15 and 16).

Variations and trends of incompatible trace elements, as well as their PM-normalized patterns, are close to those in the rocks of the Alaskan, Uralian and Arabian complexes (Figures 11E and 12A–D). Abundance of Ni varies in the same range and has the same dependence on MgO as for the Alaskan and Arabian UA-complexes (Figure 12E). Systematics of Cr are also close to the Alaskan plutons (Figure 12F).

Compositional variations of olivine and Cr-spinel partially overlap with those from Alaskan complexes and Galmoenan (Figure 9). Chemical features of clinopyroxene are very similar to those from Alaskan and Galmoenan complexes, yet the composition of clinopyroxene reported here spans a broader range towards low-Mg#, high-Al, and high-Ti compositions (Figure 7). Notably, zoning and compositional variations of clinopyroxene grains observed in the studied volcanics (Figure 8) are also typical of that of clinopyroxene from the Bridget Cove basalts, which are proposed to be volcanic counterparts for of the UA-complexes of the Alaskan belt [7].

Hence, the comparison shows that our rock assemblage shares all the characteristic features of a Ural-Alaskan type. Consequently, the studied volcano–plutonic complex is a unique example where both plutonic and volcanic suites of the UA-complex are exposed, rendering it a promising case for the petrological study of these complexes.

## 6. Conclusions

The volcano–plutonic complex of the Tumrok range (Eastern Kamchatka) is represented by the Valaginsky series volcanics and Andrianovsky pluton, which exhibit a series of co-magmatic volcanic (picrites, basalts) and intrusive (dunites, wehrlites, monzogabbros and gabbrodolerites) rocks. The parental melt of this series, estimated from compositions of chromite-hosted and olivine-hosted [61] melt inclusions, was ankaramitic ( $\text{CaO}/\text{Al}_2\text{O}_3 > 1$ ). Therefore, picrites, which have  $\text{CaO}/\text{Al}_2\text{O}_3 > 1$ , should be classified as ankaramites. Evolution of this series began with olivine + chromite crystallization, which was followed by olivine + clinopyroxene crystallization, followed by the clinopyroxene + plagioclase + K-Na-feldspar eutectic, hence representing the complete differentiation of an ankaramitic melt. Chemical and mineralogical features of this complex allow for its classification as a Ural-Alaskan type, making it a unique example of such a complex where both plutonic and volcanic facies are present.

**Supplementary Materials:** The following supporting information can be downloaded at: <https://www.mdpi.com/article/10.3390/min13010126/s1>, Table S1: chemical composition of olivine; Table S2: chemical composition of clinopyroxene; Table S3: chemical composition of chromite; Table S4: bulk chemical composition of the rocks; Table S5: chemical composition of glasses of the heated and quenched chromite-hosted melt inclusions.

**Author Contributions:** Conceptualization, I.F.C., N.I.B. and A.V.K.; methodology, I.F.C. and V.D.S.; formal analysis, N.I.B.; investigation, V.D.S. and N.I.B.; resources, A.V.K., I.F.C., V.S.K. and N.I.B.; writing—original draft preparation, I.F.C. and N.I.B.; writing—review and editing, A.A., E.V.P., A.V.K. and V.S.K.; visualization, N.I.B. and I.F.C.; supervision, V.S.K. and I.F.C.; project administration, V.S.K.; funding acquisition, V.S.K. All authors have read and agreed to the published version of the manuscript.

**Funding:** This study is fulfilled under Research program FMUF-2022-0004 of the D. S. Korzhinskii Institute of Experimental Mineralogy RAS. Field work, sample preparation and bulk chemical analyses were funded by Russian Science Foundation (project number 21-17-00122). E.V.P. was funded by Russian State scientific program AAAA-A18-118052590029-6.

**Data Availability Statement:** The data used in this study are available as Supplementary Files and also via request to the corresponding author (I.F.C.) [ivanlab211@gmail.com](mailto:ivanlab211@gmail.com).

**Acknowledgments:** The authors thank RSF project leader Michael Zelensky for providing the funding, and help with the field work organization. We are also grateful to Alexey Ivanov (Institute of the Earth's crust) and all staff who carried out bulk chemical analysis; Elizaveta Grigor'eva for providing some of the photographs used in the article; and Andrey Izokh for an informal discussion. V.D.S. acknowledges support from M. V. Lomonosov State University Program of Development.

**Conflicts of Interest:** The authors declare no conflict of interest.

## References

1. Batanova, V.; Pertsev, A.; Kamenetsky, V.; Ariskin, A.; Mochalov, A.; Sobolev, A. Crustal evolution of island-arc ultramafic magma: Galmoenan pyroxenite–dunite plutonic complex, Koryak Highland (Far East Russia). *J. Petrol.* **2005**, *46*, 1345–1366. [\[CrossRef\]](#)
2. Guillou-Frottier, L.; Burov, E.; Augé, T.; Gloaguen, E. Rheological conditions for emplacement of Ural–Alaskan-type ultramafic complexes. *Tectonophysics* **2014**, *631*, 130–145. [\[CrossRef\]](#)
3. Irvine, T.N. *The Ultramafic Complex and Related Rocks of Duke Island, Southeastern Alaska*; California Institute of Technology: Pasadena, CA, USA, 1959.
4. Levinson-Lessing, F. Geology of Ujno–Zaozersky Dacha and Denezhkin Kamen in the North Urals. *Trans. St-Petersburg Nat. Hist. Soc.* **1900**, *30*, 257.
5. Noble, J.; Taylor, H., Jr. *Correlation of the Ultramafic Complexes of Southeastern Alaska with Those of Other Parts of North America and the World: International Geological Congress, 21st*; U.S. Geological Survey Bulletin: Washington, DC, USA, 1960.
6. Himmelberg, G.R.; Loney, R.A. *Characteristics and Petrogenesis of Alaskan-Type Ultramafic-Mafic Intrusions, Southeastern Alaska*; US Government Printing Office: Washington, DC, USA, 1995.
7. Irvine, T. Bridget Cove volcanics, Juneau Area, Alaska: Possible parental magma of Alaskan-type ultramafic complexes. *Carnegie Inst. Wash. Yearb.* **1973**, *72*, 478–491.
8. Irvine, T.N. *Petrology of the Duke Island Ultramafic Complex Southeastern Alaska*; Geological Society of America: Boulder, CO, USA, 1974.
9. Johan, Z.; Cabri, L. Alaskan-type complexes and their platinum-group element mineralization. *Geol. Geochem. Mineral. Miner. Benef. Platin.-Group Elem.* **2002**, *54*, 669–719.
10. Nixon, G. Ni-Cu sulfide mineralization in the Turnagain Alaskan-type complex: A unique magmatic environment. *Geol. Surv. Br. Columbia* **1998**, *1*, 12.
11. Tisl, M.; Burgath, K.; Höndorf, A.; Kreuzer, H.; Munoz, R.; Salinas, R. Origin and emplacement of Tertiary ultramafic complexes in northwest Colombia: Evidence from geochemistry and K-Ar, Sm-Nd and Rb-Sr isotopes. *Earth Planet. Sci. Lett.* **1994**, *126*, 41–59. [\[CrossRef\]](#)
12. Anikina, E.; Malitch, K.; Pushkarev, E.; Shmelev, V. The Nizhny Tagil and Volkovsky Massifs of the Uralian Platinum Belt, and Related Deposits. In Proceedings of the 12th International Platinum Symposium, Yekaterinburg, Russia, 11–14 August 2014; p. 48.
13. Duparc, L.; Tikhonovich, M.N. *Le Platine et les gîtes Platinifères de l'Oural et du Monde*; Hachette Livre Bnf: Paris, France, 1920; p. 672. (In French)
14. Efimov, A. *Gabbro-Hyperbasite Complexes of the Urals and the Ophiolite Problem*; Nauka: Moscow, Russia, 1984; p. 232. (In Russian)
15. Fershtater, G.; Bea, F.; Pushkarev, E.; Garuti, G.; Montero, P.; Zaccarini, F. Insight into the petrogenesis of the Urals Platinum Belt: New geochemical evidence. *Geochem. Int.* **1999**, *37*, 302–319.
16. Garuti, G.; Pushkarev, E.V.; Zaccarini, F. Composition and paragenesis of Pt alloys from chromitites of the Uralian–Alaskan-type Kytlym and Uktus complexes, northern and central Urals, Russia. *Can. Mineral.* **2002**, *40*, 1127–1146. [\[CrossRef\]](#)
17. Ivanov, O. *Kontsentricheski-zonal'nye piroksenit-dunitovye massivy Urala: (Mineralogiya, petrologiya, genezis) (Concentrically Zoned Pyroxenite–Dunite Massifs of the Urals: Mineralogy, Petrology, and Genesis)*; Ural: Yekaterinburg, Russia, 1997; p. 448. (In Russian)
18. Krause, J. Petrogenetic Evolution of Uralian-Alaskan-Type Mafic-Ultramafic Complexes in the Southern and Middle Urals, Russia. Ph.D. Thesis, Mainz University, Mainz, Germany, 2008; p. 163.
19. Pushkarev, E. *Petrology of the Uktus Dunite–Clinopyroxenite–Gabbro Massif (the Middle Urals)*; The Institute of Geology and Geochemistry: Ekaterinburg, Russia, 2000; p. 71. (In Russian)
20. Stepanov, S.Y.; Palamarchuk, R.; Antonov, A.; Kozlov, A.; Varlamov, D.; Khanin, D.; Zolotarev Jr, A. Morphology, composition, and ontogenesis of platinum-group minerals in chromitites of zoned clinopyroxenite–dunite massifs of the Middle Urals. *Russ. Geol. Geophys.* **2020**, *61*, 47–67. [\[CrossRef\]](#)
21. Vysotsky, N. Platinum deposits of the Isovsky and Nizhny-Tagil districts in the Urals. *Proc. Geol. Comm. New Ser.* **1913**, *62*, 1–693.
22. Zavaritsky, A. Primary platinum deposits of the Urals. *Matér. Pour Géol. Gén. Appl. Com. Géol.* **1928**, *108*, 1–53. (In Russian)
23. Batanova, V.; Astrakhantsev, O. Tectonic position and origins of the zoned mafic-ultramafic plutons in the northern Olyutor Zone, Koryak Highlands. *Geotectonics* **1992**, *26*, 153–165.
24. Batanova, V.; Astrakhantsev, O.; Sidorov, Y.G. The dunites of the Gal'moenansk pluton, Koryak Highlands. *Int. Geol. Rev.* **1991**, *33*, 62–73. [\[CrossRef\]](#)
25. Kuttyrev, A.; Kamenetsky, V.; Sidorov, E.; Abersteiner, A.; Chubarov, V. Silicate inclusions in isoferroplatinum: Constraints on the origin of platinum mineralization in podiform chromitites. *Ore Geol. Rev.* **2020**, *119*, 103367. [\[CrossRef\]](#)

26. Kutyrev, A.; Zhirnova, T. Concentrically-zoned massifs of the Tamanvayam Group (Koryak–Kamchatka Platiniferous Belt): Structure, age, petrological and geochemical aspects. *Russ. J. Pac. Geol.* **2019**, *13*, 350–363. [[CrossRef](#)]
27. Kutyrev, A.V.; Sidorov, E.G.; Kamenetsky, V.S.; Chubarov, V.M.; Chayka, I.F.; Abersteiner, A. Platinum mineralization and geochemistry of the Matysken zoned Ural-Alaskan type complex and related placer (Far East Russia). *Ore Geol. Rev.* **2021**, *130*, 103947. [[CrossRef](#)]
28. Sidorov, E.; Kozlov, A.; Tolstykh, N. *The Galmoenan Ultrabasic Massif and Its Platinum Potential*; Nauchnyi Mir: Moscow, Russia, 2012; p. 288. (In Russian)
29. Murray, C. Zoned ultramafic complexes of the Alaskan-type: Feeder pipes of andesitic volcanoes. *Geol. Soc. Am.* **1972**, *132*, 313–335.
30. Derrick, G.M. Geology and economic potential of the Tout complex, NSW. In *Geology and Mineralization of the Fifield Platinum Province, New South Wales—Sixth International Platinum Symposium, Perth, Western Australia, Guidebook for the Pre-Symposium Field Excursion*; Elliott, S.J., Martin, A.R., Eds.; Geological Society of Australia: Perth, Australia, 1991; pp. 24–34.
31. Johan, Z.; Ohnenstetter, M.; Slansky, E.; Barron, L.; Suppel, D. Platinum mineralization in the Alaskan-type intrusive complexes near Fifield, New South Wales, Australia part 1. platinum-group minerals in clinopyroxenites of the Kelvin Grove prospect, Owendale intrusion. *Mineral. Petrol.* **1989**, *40*, 289–309. [[CrossRef](#)]
32. Spandler, C.J.; Eggins, S.M.; Arculus, R.J.; Mavrogenes, J.A. Using melt inclusions to determine parent-magma compositions of layered intrusions: Application to the Greenhills Complex (New Zealand), a platinum group minerals-bearing, island-arc intrusion. *Geology* **2000**, *28*, 991–994. [[CrossRef](#)]
33. Malich, K. Distribution of platinum-group elements in Aldan-Shield ultrabasic intrusions. *Geochem. Int.* **1990**, *27*, 113–116.
34. Razin, L. Geologic and genetic features of forsterite dunites and their platinum-group mineralization. *Econ. Geol.* **1976**, *71*, 1371–1376. [[CrossRef](#)]
35. Habtoor, A.; Ahmed, A.H.; Harbi, H. Petrogenesis of the Alaskan-type mafic–ultramafic complex in the Makkah quadrangle, western Arabian Shield, Saudi Arabia. *Lithos* **2016**, *263*, 33–51. [[CrossRef](#)]
36. Khedr, M.Z.; Arai, S. Petrology of a Neoproterozoic Alaskan-type complex from the Eastern Desert of Egypt: Implications for mantle heterogeneity. *Lithos* **2016**, *263*, 15–32. [[CrossRef](#)]
37. Pettigrew, N.T.; Hattori, K.H. The Quetico intrusions of western Superior Province: Neo-Archean examples of Alaskan/Ural-type mafic–ultramafic intrusions. *Precambrian Res.* **2006**, *149*, 21–42. [[CrossRef](#)]
38. Cabri, L.J.; Genkin, A.D. Re-examination of Pt alloys from lode and placer deposits, Urals. *Can. Mineral.* **1991**, *29*, 419–425.
39. Garuti, G.; Pushkarev, E.V.; Zaccarini, F.; Cabella, R.; Anikina, E. Chromite composition and platinum-group mineral assemblage in the Uktus Uralian-Alaskan-type complex (Central Urals, Russia). *Miner. Depos.* **2003**, *38*, 312–326. [[CrossRef](#)]
40. Johan, Z. Platinum-group minerals from placers related to the Nizhni Tagil (Middle Urals, Russia) Uralian-Alaskan-type ultramafic complex: Ore-mineralogy and study of silicate inclusions in (Pt, Fe) alloys. *Mineral. Petrol.* **2006**, *87*, 1–30. [[CrossRef](#)]
41. Stepanov, S.Y.; Palamarchuk, R.S.; Kozlov, A.V.; Khanin, D.A.; Varlamov, D.A.; Kiseleva, D.V. Platinum-group minerals of Pt-placer deposits associated with the Svetloborsky Ural-Alaskan type massif, Middle Urals, Russia. *Minerals* **2019**, *9*, 77. [[CrossRef](#)]
42. Tolstykh, N.D.; Sidorov, E.G.; Kozlov, A.P. Platinum-group minerals in lode and placer deposits associated with the Ural-Alaskan-type Gal’moenan complex, Koryak–Kamchatka platinum belt, Russia. *Can. Mineral.* **2004**, *42*, 619–630. [[CrossRef](#)]
43. Buddington, A.; Chapin, T. *Geology and Mineral Deposits of Southeastern Alaska*; Geological Survey (U.S.); Government Printing Office: Washington, DC, USA, 1929; p. 440.
44. Duparc, L.; Jerchoff, S. Recherches géologiques sur l’Oural du Nord. *Arch. Sci. Phys. Nat.* **1902**, *4*, 300–303.
45. Burg, J.-P.; Bodinier, J.-L.; Gerya, T.; Bedini, R.-M.; Boudier, F.; Dautria, J.-M.; Prikhodko, V.; Efimov, A.; Pupier, E.; Balanec, J.-L. Translithospheric mantle diapirism: Geological evidence and numerical modelling of the Kondyor zoned ultramafic complex (Russian Far-East). *J. Petrol.* **2009**, *50*, 289–321. [[CrossRef](#)]
46. James, O.B. Origin and emplacement of the ultramafic rocks of the Emigrant Gap area, California. *J. Petrol.* **1971**, *12*, 523–560. [[CrossRef](#)]
47. Irvine, T. The Duke Island ultramafic complex, southeastern Alaska. In *Ultramafic and Related Rocks*; Wiley & Sons: New York, NY, USA, 1967; pp. 84–97.
48. Krause, J.; Brüggmann, G.E.; Pushkarev, E.V. Accessory and rock forming minerals monitoring the evolution of zoned mafic–ultramafic complexes in the Central Ural Mountains. *Lithos* **2007**, *95*, 19–42. [[CrossRef](#)]
49. Spandler, C.J.; Arculus, R.J.; Eggins, S.M.; Mavrogenes, J.A.; Price, R.C.; Reay, A.J. Petrogenesis of the Greenhills Complex, Southland, New Zealand: Magmatic differentiation and cumulate formation at the roots of a Permian island-arc volcano. *Contrib. Mineral. Petrol.* **2003**, *144*, 703–721. [[CrossRef](#)]
50. Thakurta, J. Alaskan-type complexes and their associations with economic mineral deposits. In *Processes and Ore Deposits of Ultramafic-Mafic Magmas through Space and Time*; Elsevier: Amsterdam, The Netherlands, 2018; pp. 269–302.
51. Fershtater, G.; Pushkarev, E. Magmatic clinopyroxenites of the Urals and their evolution. *Izv. Akad. Nauk. SSSR Ser. Geol.* **1987**, *3*, 13–23. (In Russian)
52. Pertsev, A.; Savelieva, G. Primary magmas of Uralian Alaskan-type ultramafic complexes: Geochemical constraints deduced from mineral compositions. *Geochem. Int.* **2005**, *43*, 456–470.
53. Chaika, I.; Izokh, A. Dunites of the Inagli massif (Central Aldan), cumulates of lamproitic magma. *Russ. Geol. Geophys.* **2018**, *59*, 1450–1460. [[CrossRef](#)]

54. Kutyrev, A.V.; Kamenetsky, V.S.; Park, J.-W.; Maas, R.; Demonterova, E.I.; Antsiferova, T.N.; Ivanov, A.V.; Hwang, J.; Abersteiner, A.; Ozerov, A.Y. Primitive high-K intraoceanic arc magmas of Eastern Kamchatka: Implications for Paleo-Pacific tectonics and magmatism in the Cretaceous. *Earth-Sci. Rev.* **2021**, *220*, 103703. [[CrossRef](#)]
55. Shapiro, M.; Solov'ev, A. Formation of the Olyutorsky–Kamchatka foldbelt: A kinematic model. *Russ. Geol. Geophys.* **2009**, *50*, 668–681. [[CrossRef](#)]
56. Erlikh, E.N.; Shantser, A.E.; Kutyev, F.S. Meimechites of Eastern Kamchatka. *Izv. Akad. Nauk. SSSR Ser. Geol.* **1971**, *2*, 3–10. (In Russian)
57. Kamenetskiy, V.; Portnyagin, M.; Sobolev, A.; Danyushevskiy, L. Magna Composition and Crystallization Conditions of the Picrite-Basalt Suite in the Tumrok Ridge, East Kamchatka. *Geochem. Int.* **1993**, *30*, 58.
58. Kamenetsky, V.S. Petrology and Geochemistry of the Ultramafic Volcanics from the Eastern Kamchatka Ridges. Ph.D. Thesis, V.I. Vernadsky Institute of Geochemistry and Analytical Chemistry, Moscow, Russia, 1990; p. 148. (In Russian).
59. Zinkevich, V.; Danyushevskii, L.; Kamenetsky, V. Geology and Petrochemistry of Volcanogenic Rocks of the Tumrok Salient, Eastern Kamchatka. *Tikhookean. Geol.* **1991**, *5*, 84–98. (In Russian)
60. Badredinov, Z.; Markovskiy, B.; Tararin, I.; Ekimova, N.; Chubarov, V. Fluid–Silicate Separation of an Ultrabasic Melt into High-Potassium and Low-Potassium Fractions: Evidence from Picrites of the Late Cretaceous Ultrabasic Volcanic Complex, Eastern Kamchatka. *Russ. J. Pac. Geol.* **2018**, *12*, 408–418. [[CrossRef](#)]
61. Kamenetsky, V.; Sobolev, A.; Joron, J.-L.; Semet, M. Petrology and geochemistry of Cretaceous ultramafic volcanics from Eastern Kamchatka. *J. Petrol.* **1995**, *36*, 637–662. [[CrossRef](#)]
62. Koloskov, V.; Flerov, G.; Kovalenko, D. Late Cretaceous–Paleocene magmatic complexes of central Kamchatka: Geological settings and compositional features. *Russ. J. Pac. Geol.* **2009**, *3*, 319–337. [[CrossRef](#)]
63. Markovskii, B.; Rotman, V. *Geology and Petrology of the Ultramafic Volcanism*; Nedra: Leningrad, Russia, 1981; p. 247. (In Russian)
64. Slyadnev, B.; Shapovalenko, V.; Krikun, N.; Poletaeva, A.; Rotman, V.; Sidorenko, V.; Sidorov, E.; Surikov, S.; Khasanov, S. *State Geological Map of the Russian Federation. 1:1000000*, 3rd ed.; Ser. Koryak-Kamchatka. N-57: Petropavlovsk-Kamchatsky, Russia, 2006. (In Russian)
65. Chayka, I.F.; Kamenetsky, V.S.; Vladykin, N.V.; Kontonikas-Charos, A.; Prokopyev, I.R.; Stepanov, S.Y.; Krashenninnikov, S.P. Origin of alkali-rich volcanic and alkali-poor intrusive carbonatites from a common parental magma. *Sci. Rep.* **2021**, *11*, 1–13. [[CrossRef](#)] [[PubMed](#)]
66. Morgan, G.B.; London, D. Optimizing the electron microprobe analysis of hydrous alkali aluminosilicate glasses. *Am. Mineral.* **1996**, *81*, 1176–1185. [[CrossRef](#)]
67. Batanova, V.G.; Thompson, J.M.; Danyushevsky, L.V.; Portnyagin, M.V.; Garbe-Schönberg, D.; Hauri, E.; Kimura, J.I.; Chang, Q.; Senda, R.; Goemann, K. New olivine reference material for in situ microanalysis. *Geostand. Geoanalyt. Res.* **2019**, *43*, 453–473. [[CrossRef](#)]
68. Droop, G. A general equation for estimating Fe<sup>3+</sup> concentrations in ferromagnesian silicates and oxides from microprobe analyses, using stoichiometric criteria. *Mineral. Mag.* **1987**, *51*, 431–435. [[CrossRef](#)]
69. Pashkova, G.V.; Panteeva, S.V.; Ukhova, N.N.; Chubarov, V.M.; Finkelshtein, A.L.; Ivanov, A.V.; Asavin, A.M. Major and trace elements in meimechites–rarely occurring volcanic rocks: Developing optimal analytical strategy. *Geochem. Explor. Environ. Anal.* **2019**, *19*, 233–243. [[CrossRef](#)]
70. Panteeva, S.; Gladkochoub, D.; Donskaya, T.; Markova, V.; Sandimirova, G. Determination of 24 trace elements in felsic rocks by inductively coupled plasma mass spectrometry after lithium metaborate fusion. *Spectrochim. Acta Part B At. Spectrosc.* **2003**, *58*, 341–350. [[CrossRef](#)]
71. Warr, L.N. IMA–CNMNC approved mineral symbols. *Mineral. Mag.* **2021**, *85*, 291–320. [[CrossRef](#)]
72. Morimoto, N. Nomenclature of pyroxenes. *Mineral. Petrol.* **1988**, *39*, 55–76. [[CrossRef](#)]
73. Della-Pasqua, F.N. Primitive Ankaramitic Melts in Island Arcs: Evidence from Melt Inclusions. Ph.D. Thesis, University of Tasmania, Hobart, TAS, Australia, 1997; p. 250.
74. Della-Pasqua, F.N.; Varne, R. Primitive ankaramitic magmas in volcanic arcs: A melt-inclusion approach. *Oceanogr. Lit. Rev.* **1997**, *12*, 1473.
75. Kohut, E.J.; Stern, R.J.; Kent, A.J.; Nielsen, R.L.; Bloomer, S.H.; Leybourne, M. Evidence for adiabatic decompression melting in the Southern Mariana Arc from high-Mg lavas and melt inclusions. *Contrib. Mineral. Petrol.* **2006**, *152*, 201–221. [[CrossRef](#)]
76. Mossman, D.J.; Coombs, D.S.; Kawachi, Y.; Reay, A. High-Mg arc-ankaramitic dikes, Greenhills Complex, Southland, New Zealand. *Can. Mineral.* **2000**, *38*, 191–216. [[CrossRef](#)]
77. Pushkarev, E.; Ryazancev, A.; Gottman, I.; Degtyarev, K.; Kamenetsky, V. Ankaramite: A new type of high-magnesium and high-calcium primitive melt in the Magnitogorsk island-arc zone (southern Urals). *Dokl. Earth Sci.* **2018**, *479*, 463–467. [[CrossRef](#)]
78. Li, X.-P.; Rahn, M.; Bucher, K. Metamorphic processes in rodingites of the Zermatt-Saas ophiolites. *Int. Geol. Rev.* **2004**, *46*, 28–51. [[CrossRef](#)]
79. Salviole-Mariani, E.; Boschetti, T.; Toscani, L.; Montanini, A.; Petriglieri, J.R.; Bersani, D. Multi-stage rodingitization of ophiolitic bodies from Northern Apennines (Italy): Constraints from petrography, geochemistry and thermodynamic modelling. *Geosci. Front.* **2020**, *11*, 2103–2125. [[CrossRef](#)]

80. Kamenetsky, V.S.; Crawford, A.J.; Meffre, S. Factors controlling chemistry of magmatic spinel: An empirical study of associated olivine, Cr-spinel and melt inclusions from primitive rocks. *J. Petrol.* **2001**, *42*, 655–671. [[CrossRef](#)]
81. Barsdell, M.; Berry, R. Origin and evolution of primitive island arc ankaramites from Western Epi, Vanuatu. *J. Petrol.* **1990**, *31*, 747–777. [[CrossRef](#)]
82. Della-Pasqua, F.; Kamenetsky, V.; Gasparon, M.; Crawford, A.; Varne, R. Al-spinels in primitive arc volcanics. *Mineral. Petrol.* **1995**, *53*, 1–26. [[CrossRef](#)]
83. Foden, J. The petrology of the calcalkaline lavas of Rindjani volcano, east Sunda arc: A model for island arc petrogenesis. *J. Petrol.* **1983**, *24*, 98–130. [[CrossRef](#)]
84. Ichiyama, Y.; Ishiwatari, A. HFSE-rich picritic rocks from the Mino accretionary complex, southwestern Japan. *Contrib. Mineral. Petrol.* **2005**, *149*, 373–387. [[CrossRef](#)]
85. Thirlwall, M.; Graham, A. Evolution of high-Ca, high-Sr C-series basalts from Grenada, Lesser Antilles: The effects of intra-crustal contamination. *J. Geol. Soc.* **1984**, *141*, 427–445. [[CrossRef](#)]
86. Yang, L.; Song, S.; Su, L.; Allen, M.B.; Niu, Y.; Zhang, G.; Zhang, Y. Heterogeneous oceanic arc volcanic rocks in the South Qilian accretionary belt (Qilian Orogen, NW China). *J. Petrol.* **2019**, *60*, 85–116. [[CrossRef](#)]
87. Zhang, Z.; Zhou, G.; Kusky, T.M.; Yan, S.; Chen, B.; Zhao, L. Late Paleozoic volcanic record of the Eastern Junggar terrane, Xinjiang, Northwestern China: Major and trace element characteristics, Sr–Nd isotopic systematics and implications for tectonic evolution. *Gondwana Res.* **2009**, *16*, 201–215. [[CrossRef](#)]
88. Lyubetskaya, T.; Korenaga, J. Chemical composition of Earth’s primitive mantle and its variance: 1. Method and results. *J. Geophys. Res. Solid Earth* **2007**, *112*, B03211. [[CrossRef](#)]
89. Roedder, E. Origin and significance of magmatic inclusions. *Bull. De Mineral.* **1979**, *102*, 487–510. [[CrossRef](#)]
90. Baskin, Y. A study of authigenic feldspars. *J. Geol.* **1956**, *64*, 132–155. [[CrossRef](#)]
91. Deer, W.A. *Rock-Forming Minerals: Feldspars*; Geological Society of London: London, UK, 1978; Volume 4A, p. 992.
92. Winchester, J.A.; Floyd, P.A. Geochemical discrimination of different magma series and their differentiation products using immobile elements. *Chem. Geol.* **1977**, *20*, 325–343. [[CrossRef](#)]
93. Le Bas, M. IUGS reclassification of the high-Mg and picritic volcanic rocks. *J. Petrol.* **2000**, *41*, 1467–1470. [[CrossRef](#)]
94. Khlif, N.; Vishnevskiy, A.; Izokh, A.; Chervyakovskaya, M. Mineral Chemistry and Trace Element Composition of Clinopyroxenes from the Middle Cambrian Ust’-Sema Formation Ankaramites and Diopside Porphyry Basalts and the Related Barangol Complex Intrusions, Gorny Altai, Russia. *Minerals* **2022**, *12*, 113. [[CrossRef](#)]
95. Lacroix, A. Sur quelques roches volcaniques mélanocrates des Possessions françaises de l’océan Indien et du Pacifique. *CR Acad. Sci. Paris* **1916**, *158*, 177–183.
96. Le Maitre, R.W.; Streckeisen, A.; Zanettin, B.; Le Bas, M.; Bonin, B.; Bateman, P. *Igneous Rocks: A Classification and Glossary of Terms: Recommendations of the International Union of Geological Sciences Subcommittee on the Systematics of Igneous Rocks*; Cambridge University Press: Cambridge, UK, 2005; p. 236.
97. Middlemost, E.A. Naming materials in the magma/igneous rock system. *Earth-Sci. Rev.* **1994**, *37*, 215–224. [[CrossRef](#)]
98. Ford, C.; Russell, D.; Craven, J.; Fisk, M. Olivine-liquid equilibria: Temperature, pressure and composition dependence of the crystal/liquid cation partition coefficients for Mg, Fe<sup>2+</sup>, Ca and Mn. *J. Petrol.* **1983**, *24*, 256–266. [[CrossRef](#)]
99. Sobolev, A.; Slutsky, A. Composition and crystallisation conditions of primary melt of Siberian meimechites: Constraint on ultrabasic magmas generation. *Geol. Geophys.* **1984**, *12*, 97–110.
100. Hanski, E.; Kamenetsky, V. Chrome spinel-hosted melt inclusions in Paleoproterozoic primitive volcanic rocks, northern Finland: Evidence for coexistence and mixing of komatiitic and picritic magmas. *Chem. Geol.* **2013**, *343*, 25–37. [[CrossRef](#)]
101. Cortés, J.A.; Wilson, M.; Condliffe, E.; Francalanci, L. The occurrence of forsterite and highly oxidizing conditions in basaltic lavas from Stromboli volcano, Italy. *J. Petrol.* **2006**, *47*, 1345–1373. [[CrossRef](#)]
102. Plechov, P.Y.; Shcherbakov, V.; Nekrylov, N. Extremely magnesian olivine in igneous rocks. *Russ. Geol. Geophys.* **2018**, *59*, 1702–1717. [[CrossRef](#)]
103. Schiano, P.; Eiler, J.; Hutcheon, I.; Stolper, E. Primitive CaO-rich, silica-undersaturated melts in island arcs: Evidence for the involvement of clinopyroxene-rich lithologies in the petrogenesis of arc magmas. *Geochem. Geophys. Geosyst.* **2000**, *1*, 1999GC000032. [[CrossRef](#)]
104. Yoder, H., Jr.; Tilley, C.E. Origin of basalt magmas: An experimental study of natural and synthetic rock systems. *J. Petrol.* **1962**, *3*, 342–532. [[CrossRef](#)]
105. Kushiro, I. Regularities in the shift of liquidus boundaries in silicate systems and their significance in magma genesis. *Ann. Rept. Dir. Geophys. Lab. Carnegie Inst. Yearb.* **1973**, *72*, 497–502.
106. Presnall, D.; Dixon, S.A.; Dixon, J.R.; O’donnell, T.; Brenner, N.; Schrock, R.; Dycus, D. Liquidus phase relations on the join diopside-forsterite-anorthite from 1 atm to 20 kbar: Their bearing on the generation and crystallization of basaltic magma. *Contrib. Mineral. Petrol.* **1978**, *66*, 203–220. [[CrossRef](#)]
107. Schairer, J. Melting relations of the common rock-forming oxides. *J. Am. Ceram. Soc.* **1957**, *40*, 215–235. [[CrossRef](#)]

108. Izokh, A.E.; Vishnevskii, A.V.; Polyakov, G.V.; Kalugin, V.M.; Oyunchimeg, T.; Shelepaev, R.A.; Egorova, V.V. The Ureg Nuur Pr-bearing volcanoplutonic picrite-basalt association in the Mongolian Altay as evidence for a Cambrian-Ordovician large igneous province. *Russ. Geol. Geophys.* **2010**, *51*, 521–533. [[CrossRef](#)]
109. Khlif, N.; Vishnevskiy, A.V.; Izokh, A.E. Ankaramites of Gorny Altai: Mineralogical, petrographic and petrochemical features of diopside porphyry basalts of the Ust'-Sema Formation. *Russ. Geol. Geophys.* **2020**, *61*, 250–267. [[CrossRef](#)]

**Disclaimer/Publisher's Note:** The statements, opinions and data contained in all publications are solely those of the individual author(s) and contributor(s) and not of MDPI and/or the editor(s). MDPI and/or the editor(s) disclaim responsibility for any injury to people or property resulting from any ideas, methods, instructions or products referred to in the content.